Numer. Math. (2012) 121:165–204
DOI 10.1007/s00211-011-0427-7

Numerische Mathematik

A multipoint flux mixed finite element method on distorted quadrilaterals and hexahedra

Mary Wheeler · Guangri Xue · Ivan Yotov

Received: 14 August 2010 / Revised: 11 August 2011 / Published online: 6 November 2011

Abstract In this paper, we develop a new mixed finite element method for elliptic problems on general quadrilateral and hexahedral grids that reduces to a cell-centered finite difference scheme. A special non-symmetric quadrature rule is employed that yields a positive definite cell-centered system for the pressure by eliminating local velocities. The method is shown to be accurate on highly distorted rough quadrilateral and hexahedral grids, including hexahedra with non-planar faces. Theoretical and numerical results indicate first-order convergence for the pressure and face fluxes.

Mathematics Subject Classification (2000) 65N06 · 65N08 · 65N12 · 65N15 · 65N22 · 65N30 · 76S05

1 Introduction

Single phase incompressible flow in porous media is governed by coupled Darcy's law and continuity equation:

$$\mathbf{u} = -K\nabla p, \tag{1.1}$$

$$\nabla \cdot \mathbf{u} = f, \tag{1.2}$$

M. Wheeler · G. Xue (✉)
Center for Subsurface Modeling, Institute for Computational Engineering and Sciences, The University of Texas at Austin, 201 E 24th Street, Austin, TX 78712, USA
e-mail: gxue@ices.utexas.edu

M. Wheeler
e-mail: mfw@ices.utexas.edu

I. Yotov
Department of Mathematics, University of Pittsburgh, 301 Thackeray Hall, Pittsburgh, PA 15260, USA
e-mail: yotov@math.pitt.edu

where p is the pressure, $\mathbf{u}$ is the velocity, K represents the rock permeability divided by fluid kinematic viscosity, and f is the source term. In [33,51], a special mixed finite element (MFE) method called the multipoint flux mixed finite element (MFMFE) has been developed for elliptic problems (1.1)–(1.2). This method reduces to a cell-centered finite difference scheme for the scalar variable and is accurate for discontinuous full tensor coefficients on h^2-perturbed parallelograms, simplicial grids, and h^2-perturbed parallelepipeds. Cell-centered discretizations are very efficient and widely used for modeling complex multiphase multicomponent fluid flows in porous media, since multiscale spatial variability of the material properties often necessitate millions of cells for accurate approximations. The goal of this paper is to develop a new MFMFE method that is accurate on general quadrilaterals and hexahedra such as shown in Fig. 1. This is a typical grid encountered in geological models. Furthermore, hexahedral grids can represent highly irregular geometries with significantly reduced number of elements compared to tetrahedral grids. This is especially important in computationally intensive applications such as carbon sequestration in saline aquifers.

MFE methods [14,15,20,22,40,41,45] are well suited to discretize this coupled system, as they provide accurate and locally mass conservative velocities and can accurately treat discontinuous full tensor coefficients. A standard formulation of MFE yields a saddle point system and requires solving pressure and velocity simultaneously. Another approach, the hybrid MFE formulation [12,16], reduces the discrete problem to a symmetric positive definite system for the pressure Lagrange multipliers on element faces. In addition, efficient formulations that reduce to cell-centered pressure schemes have also been developed. These apply appropriate MFE spaces and numerical quadrature rules for the velocity mass term. Examples include [42,48] for diagonal permeability on rectangular grids based on the lowest order Raviart–Thomas MFE method [41] and the expanded mixed finite element (EMFE) method for smooth full tensor permeability on rectangular and cuboid grids [8] and smooth curvilinear grids [7]. In the case of discontinuous permeability, EMFE loses accuracy unless the pressure Lagrange multipliers are introduced along discontinuous interfaces [7]. The MFMFE

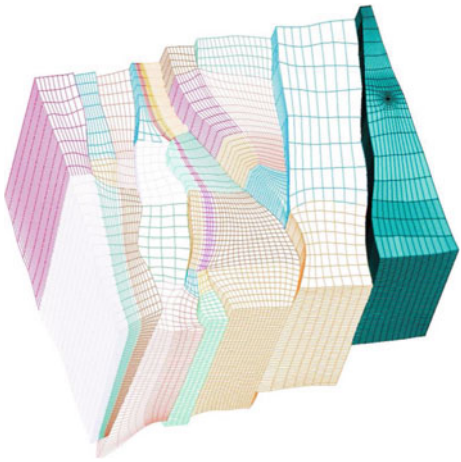

Fig. 1 General hexahedral mesh for a geological computational domain with layers and faults

method [33,51] has been designed to be a cell-centered pressure scheme that is accurate for both smooth and discontinuous full tensor permeability, but unfortunately it is not accurate on general hexahedral grids.

The velocity finite element spaces in the above mentioned MFE methods on quadrilateral and hexahedral meshes are defined via a mapping from the reference rectangle or cube using the Piola transformation [38,45]. This transformation preserves normal components of vectors and leads to continuous normal flux approximations on the physical grid. Optimal order velocity convergence in the L^2-norm on quadrilaterals has been established for the Raviart–Thomas (RT) spaces [41,45] in [11,45,47]. However, approximation accuracy for the divergence of the velocity as well as for the L^2-norm of the velocity in other MFE spaces may be reduced due to failure of the classical scaling arguments [11]. On hexahedra, the deterioration of accuracy is even more severe due the fact that the constant vector is not contained in the velocity space [39,43]. Optimal approximation and superconvergence properties in some MFE methods can be obtained under a grid restrictions to h^2-perturbed parallelograms or parallelepipeds [27,33,51]. Efforts have been made to define accurate MFE methods on highly distorted elements; proposed developments include [10,11,29,44] where new families of quadrilateral finite element spaces and lowest order hexahedral finite element spaces are obtained by enriching the classical Raviart–Thomas finite element spaces. Other approaches employ composite-element techniques, see [36,43]. All of these methods require solving saddle point problems in their standard forms.

The multipoint flux approximation (MPFA) method [3,4,24,23] has gained significant popularity since it combines the advantages of the above mentioned methods: it is accurate for rough grids and rough full tensor coefficients, and reduces to a cell-centered pressure scheme. On quadrilaterals and hexahedra the method can be formulated either on the physical space or on the reference space, leading to a a non-symmetric or symmetric scheme, respectively [3]. The method was originally developed as a non-variational finite volume method. However, the convergence analysis was performed by formulating it as a MFE method with appropriate finite element spaces and numerical quadrature rules for the local velocity elimination. In the case of quadrilaterals, this was done in [34,35] using a broken Raviart–Thomas space and in [51] using the lowest order Brezzi–Douglas–Marini (BDM_1) space. The latter work develops the MFMFE method, which is also formulated and analyzed on simplicial elements in two and three dimensions and is closely related to the MPFA method. In [33], this scheme was extended to hexahedral elements by introduction of enhanced BDDF_1 spaces. The methods in [33,34,51] use symmetric quadrature rules and are related and in some cases [1,34] equivalent to the reference space MPFA method. They were shown to be accurate on h^2-perturbed parallelograms and h^2-perturbed parallelepipeds. Similar approach has been developed on simplicial elements in [17]. The method analyzed in [35] uses a non-symmetric quadrature rule and is first order accurate on general quadrilaterals. It is shown to be equivalent to the physical space MPFA method.

In this paper we develop a new non-symmetric MFMFE method that is first order accurate on general quadrilaterals and hexahedra. As in the symmetric MFMFE method [33,50,51], we employ the lowest order BDM_1 or enhanced BDDF_1 spaces. A non-symmetric quadrature rule is introduced for the velocity mass matrix that allows for local velocity elimination and reduces the method to a cell-centered pressure

system. Unlike its symmetric variant, the quadrature rule satisfies certain critical properties on the physical elements, which are key ingredients in the analysis. The method is equivalent to the symmetric MFMFE method on cuboids and rectangles.

The quadrature rule is similar to the one proposed in [35] for quadrilateral grids. However, the analysis in [35] does not extend to three dimensions, as it relies on the approximation property of the RT_0 velocity space, which is lost on general hexahedral elements. For the same reason the analysis of the symmetric MFMFE method in [33,51] cannot be extended to general hexahedra. Motivated by the fact that the Piola transformation provides accurate interpolation of normal velocities on faces of physical elements, we employ techniques from the analysis of mimetic finite difference (MFD) methods [18,37]. In particular, we first establish $\mathcal{O}(h)$ convergence for $\|\Pi\mathbf{u} - \mathbf{u}_h\|$ (Theorem 3.1), where Π is the enhanced $BDDF_1$ mixed finite element interpolant, using critical properties on the non-symmetric quadrature (Lemmas 2.2 and 2.4) and various bounds on general hexahedra (Lemmas 3.7, 3.8, and 3.10). Next, we observe that Π preserves the normal component of constant vectors on hexahedra (Lemma 3.11) and linear vectors on quadrilaterals (Lemma 3.12). A key property here is that the Piola image of a constant vector on a physical element has a linear normal component in the reference element, which belongs to the $BDDF_1$ space. We note that such property does not hold for the RT_0 interpolant, which has a constant normal component on the reference element. This allows us to establish first order approximation of the enhanced $BDDF_1$ interpolant in a face-based L^2-norm $\|\mathbf{u} - \Pi\mathbf{u}\|_{\mathcal{F}_h}$ (Lemma 3.14), which gives first order accuracy for $\|\mathbf{u} - \mathbf{u}_h\|_{\mathcal{F}_h}$ (Theorem 3.2). Finally, the pressure error estimate (Theorem 4.3) uses the critical properties on the non-symmetric quadrature rule as well as an inf–sup condition Lemma 4.15.

Our analysis applies to hexahedra with non-planar faces and it is confirmed by the numerical experiments. Existing methods with pressure and velocity degrees of freedom similar to our method, such as MFD methods [18], composite RT_0 methods [36,43], or finite volume methods [28], are limited to planar faces or require extra tangential velocity degrees of freedom to handle non-planar faces [19].

As in the non-symmetric MPFA method on quadrilaterals [35] or the non-symmetric local flux MFD method on polyhedra [37], a coercivity condition needs to be satisfied for the well-posedness of the non-symmetric MFMFE method. The condition is similar to the ones from [35,37] and depends on the element distortion and permeability anisotropy. In our numerical examples we investigate these effects, although we emphasize the convergence of the method. We also compare the behavior of the non-symmetric MFMFE method to the symmetric version of the method, which is unconditionally positive definite. As expected, the non-symmetric method converges on rough grids, where the convergence of the symmetric method deteriorates. However, for some highly anisotropic problems, the non-symmetric method loses coercivity, while the symmetric method still works. Therefore one or the other method may be preferable, depending on the properties of the grids and the permeability coefficient. This choice can be made element by element. We refer the reader to [2,5,25,26] for more comprehensive studies of the grid aspect ratio and anisotropy effects on the monotonicity and coercivity of the closely related MPFA method, where modified methods with improved robustness have been developed. Furthermore, grid smoothing techniques (Gridpro, http://www.gridpro.com/) or a posteriori error estimation and adaptive grid

refinement [46] could be employed to improve the robustness of the MFMFE method and the solution quality.

The rest of the paper is organized as follows. In Sect. 2, the non-symmetric MFMFE method is developed. In Sects. 3 and 4, the error analysis for the velocity and pressure, respectively, is presented. In Sect. 5, numerical examples demonstrate the superior convergence properties of the non-symmetric MFMFE method compared to the symmetric MFMFE method [33,51]. Conclusions are given in Sect. 6.

Throughout the paper we use the notation $X \lesssim (\gtrsim) Y$ to denote that there exists a constant C, independent of the mesh size h, such that $X \leq (\geq) CY$. The notation $X \eqsim Y$ means that both $X \lesssim Y$ and $X \gtrsim Y$ hold.

For a domain $G \subset \mathbb{R}^d$, the $L^2(G)$ inner product and norm for scalar and vector valued functions are denoted $(\cdot,\cdot)_G$ and $\|\cdot\|_G$, respectively. The norms and seminorms of the Sobolev spaces $W^{k,p}(G)$, $k \in \mathbb{R}$, $p > 0$ are denoted by $\|\cdot\|_{k,p,G}$ and $|\cdot|_{k,p,G}$, respectively. The norms and seminorms of the Hilbert spaces $H^k(G)$ are denoted by $\|\cdot\|_{k,G}$ and $|\cdot|_{k,G}$, respectively. We omit G in the subscript if $G = \Omega$. For a section of the domain, subdomain, or element boundary $S \subset \mathbb{R}^{d-1}$ we write $\langle\cdot,\cdot\rangle_S$ and $\|\cdot\|_S$ for the $L^2(S)$ inner product (or duality pairing) and norm, respectively. For a tensor-valued function M, let $\|M\|_{k,\infty} = \max_{i,j} \|M_{ij}\|_{k,\infty}$. Furthermore, let

$$H(\mathrm{div}; G) = \left\{\mathbf{v} \in (L^2(G))^d : \nabla\cdot\mathbf{v} \in L^2(G)\right\},$$
$$\|\mathbf{v}\|_{\mathrm{div};G} = \left(\|\mathbf{v}\|_G^2 + \|\nabla\cdot\mathbf{v}\|_G^2\right)^{1/2}.$$

2 Definition of the method

We consider the system (1.1)–(1.2) in a domain $\Omega \subset \mathbb{R}^d$, $d = 2, 3$ with Lipschitz continuous boundary. For simplicity we assume homogeneous Dirichlet boundary conditions

$$p = 0 \quad \text{on } \partial\Omega,$$

although more general boundary conditions can also be treated. We assume that K is a symmetric and uniformly positive definite tensor with $L^\infty(\Omega)$ components satisfying, for some $0 < k_0 \leq k_1 < \infty$,

$$k_0\xi^T\xi \leq \xi^T K(\mathbf{x})\xi \leq k_1\xi^T\xi, \quad \forall\mathbf{x} \in \Omega, \quad \text{and } \forall\xi \in \mathbb{R}^d. \tag{2.1}$$

2.1 Finite element mappings

Let $\mathcal{T}_h$ be a conforming, shape-regular, quasi-uniform partition of Ω [21]. The elements considered are quadrilaterals and hexahedra in two and three dimensions, respectively. We assume that for any $E \in \mathcal{T}_h$ there exists a bilinear (trilinear in 3D) bijection mapping $F_E : \hat{E} \to E$, where $\hat{E}$ is the reference square (cube). Denote the Jacobian matrix by DF_E and let $J_E = \det(DF_E)$. Assume that $\mathrm{sign}(J_E) > 0$.

Denote the inverse mapping by F_E^{-1}, its Jacobian matrix by DF_E^{-1}, and let $J_{F_E^{-1}} = \det(DF_E^{-1})$. We have that

$$DF_E^{-1}(\mathbf{x}) = (DF_E)^{-1}(\hat{\mathbf{x}}), \quad J_{F_E^{-1}}(\mathbf{x}) = \frac{1}{J_E(\hat{\mathbf{x}})}.$$

In the case of hexahedra, $\hat{E}$ is the unit cube with vertices $\hat{\mathbf{r}}_1 = (0,0,0)^T$, $\hat{\mathbf{r}}_2 = (1,0,0)^T$, $\hat{\mathbf{r}}_3 = (1,1,0)^T$, $\hat{\mathbf{r}}_4 = (0,1,0)^T$, $\hat{\mathbf{r}}_5 = (0,0,1)^T$, $\hat{\mathbf{r}}_6 = (1,0,1)^T$, $\hat{\mathbf{r}}_7 = (1,1,1)^T$, $\hat{\mathbf{r}}_8 = (0,1,1)^T$. Denote by $\mathbf{r}_i = (x_i, y_i, z_i)^T$, $i = 1, \ldots, 8$, the eight corresponding vertices of element E as shown in Fig. 2. We note that the element can have non-planar faces. The outward unit normal vectors to the faces of E and $\hat{E}$ are denoted by $\mathbf{n}_i$ and $\hat{\mathbf{n}}_i$, $i = 1, \ldots, 6$, respectively. In this case F_E is a trilinear mapping given for $\hat{\mathbf{x}} = (\hat{x}, \hat{y}, \hat{z}) \in \hat{E}$ by

$$\begin{aligned} F_E(\hat{\mathbf{x}}) &= \mathbf{r}_1(1-\hat{x})(1-\hat{y})(1-\hat{z}) + \mathbf{r}_2\hat{x}(1-\hat{y})(1-\hat{z}) + \mathbf{r}_3\hat{x}\hat{y}(1-\hat{z}) \\ &\quad + \mathbf{r}_4(1-\hat{x})\hat{y}(1-\hat{z}) + \mathbf{r}_5(1-\hat{x})(1-\hat{y})\hat{z} + \mathbf{r}_6\hat{x}(1-\hat{y})\hat{z} \\ &\quad + \mathbf{r}_7\hat{x}\hat{y}\hat{z} + \mathbf{r}_8(1-\hat{x})\hat{y}\hat{z} \\ &= \mathbf{r}_1 + \mathbf{r}_{21}\hat{x} + \mathbf{r}_{41}\hat{y} + \mathbf{r}_{51}\hat{z} + (\mathbf{r}_{34} - \mathbf{r}_{21})\hat{x}\hat{y} + (\mathbf{r}_{65} - \mathbf{r}_{21})\hat{x}\hat{z} \\ &\quad + (\mathbf{r}_{85} - \mathbf{r}_{41})\hat{y}\hat{z} + (\mathbf{r}_{21} - \mathbf{r}_{34} - \mathbf{r}_{65} + \mathbf{r}_{78})\hat{x}\hat{y}\hat{z}, \end{aligned} \tag{2.2}$$

where $\mathbf{r}_{ij} = \mathbf{r}_i - \mathbf{r}_j$. It is easy to see that each component of DF_E is a bilinear function of two space variables:

$$\begin{aligned} DF_E(\hat{\mathbf{x}}) = [&\mathbf{r}_{21} + (\mathbf{r}_{34} - \mathbf{r}_{21})\hat{y} + (\mathbf{r}_{65} - \mathbf{r}_{21})\hat{z} + (\mathbf{r}_{21} - \mathbf{r}_{34} - \mathbf{r}_{65} + \mathbf{r}_{78})\hat{y}\hat{z}, \\ &\mathbf{r}_{41} + (\mathbf{r}_{34} - \mathbf{r}_{21})\hat{x} + (\mathbf{r}_{85} - \mathbf{r}_{41})\hat{z} + (\mathbf{r}_{21} - \mathbf{r}_{34} - \mathbf{r}_{65} + \mathbf{r}_{78})\hat{x}\hat{z}, \\ &\mathbf{r}_{51} + (\mathbf{r}_{65} - \mathbf{r}_{21})\hat{x} + (\mathbf{r}_{85} - \mathbf{r}_{41})\hat{y} + (\mathbf{r}_{21} - \mathbf{r}_{34} - \mathbf{r}_{65} + \mathbf{r}_{78})\hat{x}\hat{y}]. \end{aligned} \tag{2.3}$$

In the case of quadrilaterals, $\hat{E}$ is the unit square with vertices $\hat{\mathbf{r}}_1 = (0,0)^T$, $\hat{\mathbf{r}}_2 = (1,0)^T$, $\hat{\mathbf{r}}_3 = (1,1)^T$, $\hat{\mathbf{r}}_4 = (0,1)^T$. Let $\mathbf{r}_i$, $i = 1, \ldots, 4$, be the corresponding vertices of E. The bilinear mapping of quadrilaterals has the form, for $\hat{\mathbf{x}}(\hat{x}, \hat{y}) \in \hat{E}$,

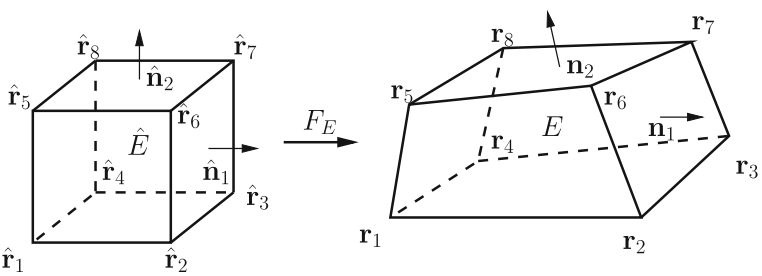

Fig. 2 Trilinear hexahedral mapping

$$\begin{aligned} F_E(\hat{\mathbf{x}}) &= \mathbf{r}_1(1-\hat{x})(1-\hat{y}) + \mathbf{r}_2\hat{x}(1-\hat{y}) + \mathbf{r}_3\hat{x}\hat{y} + \mathbf{r}_4(1-\hat{x})\hat{y} \\ &= \mathbf{r}_1 + (\mathbf{r}_2-\mathbf{r}_1)\hat{x} + (\mathbf{r}_4-\mathbf{r}_1)\hat{y} + (\mathbf{r}_3+\mathbf{r}_1-\mathbf{r}_2-\mathbf{r}_4)\hat{x}\hat{y}. \end{aligned} \tag{2.4}$$

The Jacobian matrix and its determinant are

$$DF_E(\hat{\mathbf{x}}) = [\mathbf{r}_2-\mathbf{r}_1+(\mathbf{r}_3+\mathbf{r}_1-\mathbf{r}_2-\mathbf{r}_4)\hat{y}, \mathbf{r}_4-\mathbf{r}_1+(\mathbf{r}_3+\mathbf{r}_1-\mathbf{r}_2-\mathbf{r}_4)\hat{x}], \tag{2.5}$$

$$J_E = 2|T_1| + 2(|T_2|-|T_1|)\hat{x} + 2(|T_4|-|T_1|)\hat{y}, \tag{2.6}$$

where $|T_i|$ is the area of the triangle formed by the two edges sharing $\mathbf{r}_i$.

Using the above mapping definitions and the classical formula, for scalar $\phi(\mathbf{x}) = \hat{\phi}(\hat{\mathbf{x}})$, $\nabla\phi = (DF_E^{-1})^T\hat{\nabla}\hat{\phi}$, it is easy to see that, for any face or edge $e_i \subset E$,

$$\mathbf{n}_i = \frac{1}{J_{e_i}} J_E (DF_E^{-1})^T \hat{\mathbf{n}}_i, \quad J_{e_i} = |J_E (DF_E^{-1})^T \hat{\mathbf{n}}_i|_{\mathbb{R}^d}, \tag{2.7}$$

where $|\cdot|_{\mathbb{R}^d}$ is the Euclidean norm in $\mathbb{R}^d$. Also, the shape regularity and quasiuniformity of the grids imply that, for all $E \in \mathcal{T}_h$,

$$\begin{aligned} &\|DF_E\|_{0,\infty,\hat{E}} \lesssim h, \qquad \|DF_E^{-1}\|_{0,\infty,E} \lesssim h^{-1}, \\ &\|J_E\|_{0,\infty,\hat{E}} \eqsim h^d, \qquad \|J_{F_E^{-1}}\|_{0,\infty,E} \eqsim h^{-d}. \end{aligned} \tag{2.8}$$

2.2 Mixed finite element spaces

Let $\hat{\mathbf{V}}(\hat{E})$ and $\hat{W}(\hat{E})$ be the finite element spaces on the reference element $\hat{E}$. For convenience, we use the same notation in two and three dimensions.

On the reference square, let $\hat{\mathbf{V}}(\hat{E}) \times \hat{W}(\hat{E})$ be the lowest order BDM_1 finite element space [15]:

$$\begin{aligned} \hat{\mathbf{V}}(\hat{E}) &= (P_1(\hat{E}))^2 + r\,\mathrm{curl}(\hat{x}^2\hat{y}) + s\,\mathrm{curl}(\hat{x}\hat{y}^2), \\ \hat{W}(\hat{E}) &= P_0(\hat{E}), \end{aligned} \tag{2.9}$$

where r and s are real constants and $(P_k)^d$ denotes the space of d-dimensional polynomials of degree $\le k$. In the case of the unit cube, the space is defined by the enhanced BDDF_1 space [33]:

$$\begin{aligned} \hat{\mathbf{V}}(\hat{E}) &= \mathrm{BDDF}_1(\hat{E}) + r_2\mathrm{curl}(0,0,\hat{x}^2\hat{z})^T + r_3\mathrm{curl}(0,0,\hat{x}^2\hat{y}\hat{z})^T \\ &\quad + s_2\mathrm{curl}(\hat{x}\hat{y}^2,0,0)^T + s_3\mathrm{curl}(\hat{x}\hat{y}^2\hat{z},0,0)^T \\ &\quad + t_2\mathrm{curl}(0,\hat{y}\hat{z}^2,0)^T + t_3\mathrm{curl}(0,\hat{x}\hat{y}\hat{z}^2,0)^T, \\ \hat{W}(\hat{E}) &= P_0(\hat{E}), \end{aligned} \tag{2.10}$$

where the BDDF_1 velocity spaces on the unit cube [14] is defined as

$$\begin{aligned}\mathrm{BDDF}_1(\hat{E}) = (P_1(\hat{E}))^3 &+ r_0\mathrm{curl}(0,0,\hat{x}\hat{y}\hat{z})^T + r_1\mathrm{curl}(0,0,\hat{x}\hat{y}^2)^T \\ &+ s_0\mathrm{curl}(\hat{x}\hat{y}\hat{z},0,0)^T + s_1\mathrm{curl}(\hat{y}\hat{z}^2,0,0)^T \\ &+ t_0\mathrm{curl}(0,\hat{x}\hat{y}\hat{z},0)^T + t_1\mathrm{curl}(0,\hat{x}^2\hat{z},0)^T. \end{aligned} \tag{2.11}$$

Here $r_i, s_i, t_i, (i = 0, \ldots, 3)$ are real constants. Note that in both cases

$$\hat{\nabla}\cdot\hat{\mathbf{V}}(\hat{E}) = \hat{W}(\hat{E}),$$

and that for all $\hat{\mathbf{v}} \in \hat{V}(\hat{E})$ and for any face (or edge) $\hat{e}$ of $\hat{E}$,

$$\hat{\mathbf{v}}\cdot\hat{\mathbf{n}}_{\hat{e}} \in P_1(\hat{e}) \text{ on the unit square}, \quad \hat{\mathbf{v}}\cdot\hat{\mathbf{n}}_{\hat{e}} \in Q_1(\hat{e}) \text{ on the unit cube},$$

where Q_1 is the space of bilinear functions. The degrees of freedom of $\hat{\mathbf{V}}(\hat{E})$ are chosen to be the values of $\hat{\mathbf{v}}\cdot\hat{\mathbf{n}}_{\hat{e}}$ at the corners of $\hat{e}$ for all faces (or edges) of $\hat{E}$.

The spaces $\mathbf{V}(E)$ and $W(E)$ on any physical element $E \in \mathcal{T}_h$ are defined via the Piola transformation:

$$\mathbf{v} \leftrightarrow \hat{\mathbf{v}} : \mathbf{v} = \frac{1}{J_E} DF_E\hat{\mathbf{v}} \circ F_E^{-1}, \tag{2.12}$$

and the standard scalar transformation

$$w \leftrightarrow \hat{w} : w = \hat{w} \circ F_E^{-1}. \tag{2.13}$$

Under these transformations, the normal components of the velocity vectors on the faces (edges) are preserved [16]:

$$(\nabla\cdot\mathbf{v}, w)_E = (\hat{\nabla}\cdot\hat{\mathbf{v}}, \hat{w})_{\hat{E}} \quad \text{and} \quad \langle\mathbf{v}\cdot\mathbf{n}_e, w\rangle_e = \langle\hat{\mathbf{v}}\cdot\hat{\mathbf{n}}_{\hat{e}}, \hat{w}\rangle_{\hat{e}}. \tag{2.14}$$

In addition, (2.7) implies that

$$\mathbf{v}\cdot\mathbf{n}_e = \frac{1}{J_e}\hat{\mathbf{v}}\cdot\hat{\mathbf{n}}_{\hat{e}} \circ F_E^{-1}(\mathbf{x}), \tag{2.15}$$

and (2.14) implies that

$$\nabla\cdot\mathbf{v} = \left(\frac{1}{J_E}\hat{\nabla}\cdot\hat{\mathbf{v}}\right) \circ F_E^{-1}(\mathbf{x}). \tag{2.16}$$

Clearly, for $\mathbf{v} \in \mathbf{V}(E)$, $\nabla\cdot\mathbf{v} \neq$ constant since J_E is not constant on quadrilaterals or hexahedra. Furthermore, while $J_e = |e| =$ constant on quadrilaterals, this is not true on hexahedra. As a result $\mathbf{v}\cdot\mathbf{n}_e \in P_1(e)$ on quadrilaterals, but $\mathbf{v}\cdot\mathbf{n}_e \notin Q_1(e)$ on hexahedra.

The finite element spaces $\mathbf{V}_h$ and W_h are given by

$$\begin{aligned} \mathbf{V}_h &= \left\{ \mathbf{v} \in \mathbf{V} : \quad \mathbf{v}|_E \leftrightarrow \hat{\mathbf{v}},\ \hat{\mathbf{v}} \in \hat{\mathbf{V}}(\hat{E}), \quad \forall E \in \mathcal{T}_h \right\}, \\ W_h &= \left\{ w \in W : \quad w|_E \leftrightarrow \hat{w},\ \hat{w} \in \hat{W}(\hat{E}), \quad \forall E \in \mathcal{T}_h \right\}, \end{aligned} \tag{2.17}$$

where

$$\mathbf{V} = H(\mathrm{div};\Omega) = \left\{ \mathbf{v} \in (L^2(\Omega))^d : \nabla \cdot \mathbf{v} \in L^2(\Omega) \right\}, \quad W = L^2(\Omega).$$

Recall the projection operator in the space $\mathbf{V}_h$. The operator $\hat{\Pi} : (H^1(\hat{E}))^d \to \hat{\mathbf{V}}(\hat{E})$ is defined locally on each element by

$$\langle (\hat{\Pi}\hat{\mathbf{q}} - \hat{\mathbf{q}}) \cdot \hat{\mathbf{n}}_{\hat{e}}, \hat{q}_1 \rangle_{\hat{e}} = 0, \quad \forall \hat{e} \subset \partial \hat{E}, \tag{2.18}$$

where $\hat{q}_1 \in P_1(\hat{e})$ for the case of the unit square $\hat{E}$, and $\hat{q}_1 \in Q_1(\hat{e})$ for the case of the unit cube $\hat{E}$. The global operator $\Pi : \mathbf{V} \cap (H^1(\Omega))^d \to \mathbf{V}_h$ on each element E is defined by the Piola transformation:

$$\Pi\mathbf{q} \leftrightarrow \widehat{\Pi\mathbf{q}}, \quad \widehat{\Pi\mathbf{q}} = \hat{\Pi}\hat{\mathbf{q}}. \tag{2.19}$$

Furthermore, (2.15) and (2.18) imply that $\Pi\mathbf{q} \cdot \mathbf{n}$ is continuous across element interfaces, which gives $\Pi\mathbf{q} \in \mathbf{V}_h$, and (2.16) implies that

$$(\nabla \cdot (\Pi\mathbf{q} - \mathbf{q}), w) = 0, \quad \forall w \in W_h. \tag{2.20}$$

In the analysis, we will require a similar projection operator onto the lowest order Raviart–Thomas velocity space [40,41]. The RT_0 spaces are defined on the unit cube as

$$\hat{\mathbf{V}}^R(\hat{E}) = \begin{pmatrix} \alpha_1 + \beta_1 \hat{x} \\ \alpha_2 + \beta_2 \hat{y} \\ \alpha_3 + \beta_3 \hat{z} \end{pmatrix}, \qquad \hat{W}^R(\hat{E}) = P_0(\hat{E}), \tag{2.21}$$

and on the unit square as

$$\hat{\mathbf{V}}^R(\hat{E}) = \begin{pmatrix} \alpha_1 + \beta_1 \hat{x} \\ \alpha_2 + \beta_2 \hat{y} \end{pmatrix}, \qquad \hat{W}^R(\hat{E}) = P_0(\hat{E}). \tag{2.22}$$

Here α_i and β_i $(i = 1, 2, 3)$ are real constants. In both cases, $\hat{\nabla} \cdot \hat{\mathbf{V}}^R(\hat{E}) = \hat{W}^R(\hat{E})$ and $\hat{\mathbf{v}} \cdot \hat{\mathbf{n}}_{\hat{e}} \in P_0(\hat{e})$. The degrees of freedom of $\hat{\mathbf{V}}^R(\hat{E})$ are chosen to be the constant values of $\hat{\mathbf{v}} \cdot \hat{\mathbf{n}}_{\hat{e}}$ on all faces (or edges) of $\hat{E}$. The projection operator $\hat{\Pi}_R : (H^1(\hat{E}))^d \to \hat{\mathbf{V}}_R(\hat{E})$ satisfies

$$\langle (\hat{\Pi}_R\hat{\mathbf{q}} - \hat{\mathbf{q}}) \cdot \hat{\mathbf{n}}_{\hat{e}}, \hat{q}_0 \rangle_{\hat{e}} = 0, \quad \forall \hat{e} \subset \partial \hat{E}, \quad \forall \hat{q}_0 \in P_0(\hat{E}). \tag{2.23}$$

The spaces $\mathbf{V}_h^R$ and W_h^R on $\mathcal{T}_h$ and the projection operator $\Pi_R : (H^1(\Omega))^d \to \mathbf{V}_h^R$ are defined similarly to the case of $\mathbf{V}_h$ and W_h. By definition, we have

$$\mathbf{V}_h^R \subset \mathbf{V}_h, \qquad W_h^R = W_h. \tag{2.24}$$

The projection operator Π_R satisfies

$$(\nabla \cdot (\Pi_R \mathbf{q} - \mathbf{q}), w) = 0, \quad \forall w \in W_h^R, \tag{2.25}$$

and

$$\nabla \cdot \mathbf{v} = \nabla \cdot \Pi_R \mathbf{v}, \quad \forall \mathbf{v} \in \mathbf{V}_h. \tag{2.26}$$

It has been shown in [11,33,47] that on general quadrilaterals and h^2-perturbed parallelepipeds,

$$\|\mathbf{q} - \Pi \mathbf{q}\| + \|\mathbf{q} - \Pi_R \mathbf{q}\| = O(h).$$

However, on general hexahedra, it only holds that [29,39,43]

$$\|\mathbf{q} - \Pi \mathbf{q}\| + \|\mathbf{q} - \Pi_R \mathbf{q}\| = O(1).$$

Due to the above property, the analysis in [35] of the non-symmetric MPFA method on quadrilaterals does not extend to hexahedra.

Let $\hat{Q}$ be the $L^2(\hat{E})$-orthogonal projection onto $\hat{W}(\hat{E})$, satisfying for any $\hat{\varphi} \in L^2(\hat{E})$,

$$(\hat{\varphi} - \hat{Q}\,\hat{\varphi}, \hat{w})_{\hat{E}} = 0, \quad \forall\, \hat{w} \in \hat{W}(\hat{E}).$$

Let $\mathcal{Q}_h : L^2(\Omega) \to W_h$ be the projection operator satisfying for any $\varphi \in L^2(\Omega)$,

$$\mathcal{Q}_h \varphi = \hat{Q}\hat{\varphi} \circ F_E^{-1} \quad \text{on all } E.$$

It is easy to see that, due to (2.14),

$$(\varphi - \mathcal{Q}_h \varphi, \nabla \cdot \mathbf{v}) = 0, \quad \forall\, \mathbf{v} \in \mathbf{V}_h. \tag{2.27}$$

Using a scaling argument and the Bramble–Hilbert lemma [21], it can be shown that

$$\|\varphi - \mathcal{Q}_h \varphi\| \lesssim h|\varphi|_1. \tag{2.28}$$

2.3 Quadrature rule

The integration for the velocity mass matrix on any element E is performed by mapping to the reference element $\hat{E}$ and applying quadrature rule defined on $\hat{E}$. Using (2.17) and (2.12), we map the physical integral to the reference one; namely for all $\mathbf{q}, \mathbf{v} \in \mathbf{V}_h$, we have

$$(K^{-1}\mathbf{q}, \mathbf{v})_E = \left(\frac{1}{J_E} DF_E^T K^{-1}(F_E(\hat{\mathbf{x}})) DF_E \hat{\mathbf{q}}, \hat{\mathbf{v}}\right)_{\hat{E}} \equiv (\mathcal{M}_E \hat{\mathbf{q}}, \hat{\mathbf{v}})_{\hat{E}},$$

where

$$\mathcal{M}_E(\hat{\mathbf{x}}) = \frac{1}{J_E(\hat{\mathbf{x}})} DF_E^T(\hat{\mathbf{x}}) K^{-1}(F_E(\hat{\mathbf{x}})) DF_E(\hat{\mathbf{x}}). \tag{2.29}$$

Define a constant matrix $\overline{K}_E$ such that $\overline{K}_E^{ij}$ is the mean value of K^{ij} on E, where $\overline{K}_E^{ij}$ and K^{ij} denote the elements on the i-th row and j-th column of matrix $\overline{K}_E$ and K respectively. Let $\hat{\mathbf{r}}_{c,\hat{E}}$ denote the center of mass of $\hat{E}$. Replacing DF_E^T and K by the constant matrices $DF_E^T(\hat{\mathbf{r}}_{c,\hat{E}})$ and $\overline{K}_E$ respectively, we define

$$\widetilde{\mathcal{M}}_E(\hat{\mathbf{x}}) = \frac{1}{J_E(\hat{\mathbf{x}})} DF_E^T(\hat{\mathbf{r}}_{c,\hat{E}}) \overline{K}_E^{-1} DF_E(\hat{\mathbf{x}}). \tag{2.30}$$

In addition, we use $(\cdot,\cdot)_{\hat{Q},\hat{E}}$ to denote the trapezoidal rule on $\hat{E}$:

$$(\hat{\mathbf{q}}, \hat{\mathbf{v}})_{\hat{Q},\hat{E}} \equiv \frac{|\hat{E}|}{2^d} \sum_{i=1}^{2^d} \hat{\mathbf{q}}(\hat{\mathbf{r}}_i) \cdot \hat{\mathbf{v}}(\hat{\mathbf{r}}_i), \tag{2.31}$$

where $\hat{\mathbf{r}}_i$ are the vertices of element $\hat{E}$ defined in Sect. 2.1.

The quadrature rule on an element E is defined as

$$(K^{-1}\mathbf{q}, \mathbf{v})_{Q,E} \equiv (\widetilde{\mathcal{M}}_E \hat{\mathbf{q}}, \hat{\mathbf{v}})_{\hat{Q},\hat{E}} = \frac{|\hat{E}|}{2^d} \sum_{i=1}^{2^d} \widetilde{\mathcal{M}}_E(\hat{\mathbf{r}}_i) \hat{\mathbf{q}}(\hat{\mathbf{r}}_i) \cdot \hat{\mathbf{v}}(\hat{\mathbf{r}}_i). \tag{2.32}$$

Mapping back to the physical element E, we have the quadrature rule on E:

$$(K^{-1}\mathbf{q}, \mathbf{v})_{Q,E} = \frac{1}{2^d} \sum_{i=1}^{2^d} J_E(\hat{\mathbf{r}}_i)(DF_E^{-1})^T(\mathbf{r}_i) DF_E^T(\hat{\mathbf{r}}_{c,\hat{E}}) \overline{K}_E^{-1} \mathbf{q}(\mathbf{r}_i) \cdot \mathbf{v}(\mathbf{r}_i). \tag{2.33}$$

This is related to a non-symmetric inner product used in mimetic finite difference methods [32,37]. Note that this trapezoidal rule for the modified integrand induces a non-symmetric quadrature rule unless the Jacobian matrix DF_E is constant. A similar quadrature rule on quadrilateral elements was introduced in [35], where the mean value of K_E^{-1} was used. Our choice of $\overline{K}_E^{-1}$ slightly simplifies the error analysis. However, our analysis easily extends to the case of $\overline{K_E^{-1}}$, see Remark 4.6.

The global quadrature rule on Ω is defined as

$$(K^{-1}\mathbf{q}, \mathbf{v})_Q \equiv \sum_{E \in \mathcal{T}_h} (K^{-1}\mathbf{q}, \mathbf{v})_{Q,E}.$$

Remark 2.1 The quadrature rule (2.33) becomes symmetric on parallelograms and parallelepipeds. In such cases and when the permeability is a constant tensor in each element, the method is equivalent to the symmetric MFMFE method [33,51], where the quadrature rule is based on $\mathcal{M}_E$.

Next we discuss a property of the quadrature rule that leads to a cell-centered pressure scheme. The corner vector $\hat{\mathbf{q}}(\hat{\mathbf{r}}_i)$ is uniquely determined by its normal components to the faces that share the vertex. Since we chose the velocity degrees of freedom as the normal components to the face (edge) at each corner $\hat{\mathbf{r}}_i$, the corner vector $\hat{\mathbf{q}}(\hat{\mathbf{r}}_i)$ can be uniquely expressed in terms of the degrees of freedom that share the vertex $\hat{\mathbf{r}}_i$. More precisely,

$$\hat{\mathbf{q}}(\hat{\mathbf{r}}_i) = \sum_{j=1}^{d} \hat{\mathbf{q}} \cdot \hat{\mathbf{n}}_{ij}(\hat{\mathbf{r}}_i)\hat{\mathbf{n}}_{ij},$$

where $\hat{\mathbf{n}}_{ij}$, $j = 1, \ldots, d$, are the outward unit normal vectors to the faces (or edges) sharing $\hat{\mathbf{r}}_i$, and $\hat{\mathbf{q}}\cdot\hat{\mathbf{n}}_{ij}(\hat{\mathbf{r}}_i)$ are the velocity degrees of freedom associated with this corner. More precisely, the first index i denotes the node and the second index j denotes the direction. Denote the basis functions associated with $\hat{\mathbf{r}}_i$ by $\hat{\mathbf{v}}_{ij}$, $j = 1, \ldots, d$, see Fig. 3:

$$\hat{\mathbf{v}}_{ij} \cdot \hat{\mathbf{n}}_{ij}(\hat{\mathbf{r}}_i) = 1, \quad \hat{\mathbf{v}}_{ij} \cdot \hat{\mathbf{n}}_{ik}(\hat{\mathbf{r}}_i) = 0, k \neq j, \quad \hat{\mathbf{v}}_{ij} \cdot \hat{\mathbf{n}}_{lk}(\hat{\mathbf{r}}_l) = 0, \quad l \neq i, \quad k = 1, \ldots, d.$$

The quadrature rule (2.32) couples only the d basis functions associated with a corner. For example, on the unit cube,

$$(\widetilde{\mathcal{M}}_E\hat{\mathbf{v}}_{11}, \hat{\mathbf{v}}_{11})_{\hat{Q},\hat{E}} = \frac{\widetilde{\mathcal{M}}_E^{11}(\hat{\mathbf{r}}_1)}{8}, \quad (\widetilde{\mathcal{M}}_E\hat{\mathbf{v}}_{11}, \hat{\mathbf{v}}_{12})_{\hat{Q},\hat{E}} = \frac{\widetilde{\mathcal{M}}_E^{21}(\hat{\mathbf{r}}_1)}{8},$$
$$(\widetilde{\mathcal{M}}_E\hat{\mathbf{v}}_{11}, \hat{\mathbf{v}}_{13})_{\hat{Q},\hat{E}} = \frac{\widetilde{\mathcal{M}}_E^{31}(\hat{\mathbf{r}}_1)}{8}, \quad \text{and } (\widetilde{\mathcal{M}}_E\hat{\mathbf{v}}_{11}, \hat{\mathbf{v}}_{ij})_{\hat{Q},\hat{E}} = 0, \tag{2.34}$$

where $i \neq 1$, $j = 1, 2, 3$.

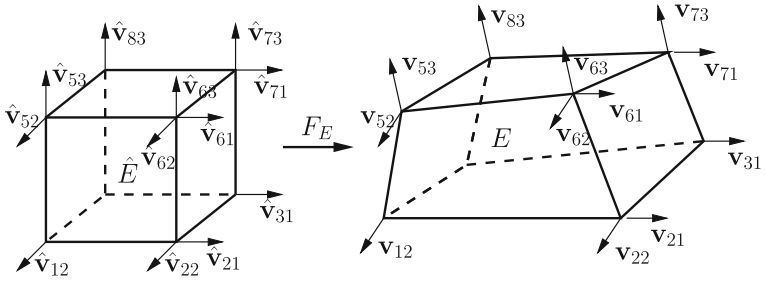

Fig. 3 Degrees of freedom and basis functions for the enhanced BDDF_1 velocity space on hexahedra

The following are some properties of the quadrature rule that are key ingredients in the velocity error analysis.

Lemma 2.1 ([33,51]) *For any* $\hat{\mathbf{v}} \in \hat{V}(\hat{E})$ *and constant vector* $\hat{\mathbf{q}}_0$ *on* $\hat{E}$*, the numerical quadrature rule satisfies*

$$(\hat{\mathbf{v}} - \hat{\Pi}_R \hat{\mathbf{v}}, \hat{\mathbf{q}}_0)_{\hat{Q},\hat{E}} = 0. \tag{2.35}$$

Lemma 2.2 *For any constant vector* $\mathbf{q}_0$ *on* E *and* $\mathbf{v} \in \mathbf{V}_h(E)$*,*

$$(K^{-1}\mathbf{q}_0, \mathbf{v} - \Pi_R \mathbf{v})_{Q,E} = 0. \tag{2.36}$$

Proof By the definition (2.32) of the quadrature rule and the Piola transformation (2.12),

$$\begin{aligned}(K^{-1}\mathbf{q}_0, \mathbf{v} - \Pi_R \mathbf{v})_{Q,E} &= (\widetilde{\mathcal{M}}_E \hat{\mathbf{q}}_0, \hat{\mathbf{v}} - \hat{\Pi}_R \hat{\mathbf{v}})_{\hat{Q},\hat{E}} \\ &= \left(\frac{1}{J_E} DF_E^T(\hat{\mathbf{r}}_{c,\hat{E}}) \overline{K}_E^{-1} DF_E J_E DF_E^{-1} \mathbf{q}_0, \hat{\mathbf{v}} - \hat{\Pi}_R \hat{\mathbf{v}}\right)_{\hat{Q},\hat{E}} \\ &= \left(DF_E^T(\hat{\mathbf{r}}_{c,\hat{E}}) \overline{K}_E^{-1} \mathbf{q}_0, \hat{\mathbf{v}} - \hat{\Pi}_R \hat{\mathbf{v}}\right)_{\hat{Q},\hat{E}} = 0, \end{aligned} \tag{2.37}$$

where we have used (2.35) in the last equality. □

Lemma 2.3 *For any constant vector* $\mathbf{q}_0$ *on* $\hat{E}$ *and* $\hat{\mathbf{v}} \in RT_0(\hat{E})$*,*

$$(DF_E(\hat{\mathbf{r}}_{c,\hat{E}})\hat{\mathbf{v}}, \mathbf{q}_0)_{\hat{E}} = (DF_E \hat{\mathbf{v}}, \mathbf{q}_0)_{\hat{E}}. \tag{2.38}$$

Proof Since the proofs in two and three dimensions are very similar, we give only the proof for the 3D case. Let $\hat{\mathbf{v}} = [\hat{v}_1(\hat{x}), \hat{v}_2(\hat{y}), \hat{v}_3(z)]^T$, $\hat{\mathbf{r}}_{c,\hat{E}} = (\hat{x}_c, \hat{y}_c, \hat{z}_c)$, and $DF_E = [\boldsymbol{\xi}_1(\hat{y}, \hat{z}), \boldsymbol{\xi}_2(\hat{x}, \hat{z}), \boldsymbol{\xi}_3(\hat{x}, \hat{y})]$,. We have

$$\begin{aligned}(DF_E \hat{\mathbf{v}}, \mathbf{q}_0)_{\hat{E}} = &\int_{\hat{E}} \hat{v}_1(\hat{x}) \boldsymbol{\xi}_1(\hat{y}, \hat{z}) \cdot \mathbf{q}_0 \, d\hat{x} d\hat{y} d\hat{z} \\ &+ \int_{\hat{E}} \hat{v}_2(\hat{y}) \boldsymbol{\xi}_2(\hat{x}, \hat{z}) \cdot \mathbf{q}_0 \, d\hat{x} d\hat{y} d\hat{z} + \int_{\hat{E}} \hat{v}_3(\hat{z}) \boldsymbol{\xi}_3(\hat{x}, \hat{y}) \cdot \mathbf{q}_0 \, d\hat{x} d\hat{y} d\hat{z}. \end{aligned} \tag{2.39}$$

Since the midpoint quadrature rule is exact for bilinear functions on a square, the first term in the right in (2.39) can be written as

$$\int_{\hat{E}} \hat{v}_1(\hat{x})\boldsymbol{\xi}_1(\hat{y},\hat{z})\cdot\mathbf{q}_0\,d\hat{x}d\hat{y}d\hat{z} = \int_0^1 \hat{v}_1(\hat{x})d\hat{x}\int_0^1\int_0^1 \boldsymbol{\xi}_1(\hat{y},\hat{z})\cdot\mathbf{q}_0\,d\hat{y}d\hat{z}$$
$$= \int_0^1 \hat{v}_1(\hat{x})\,d\hat{x}\int_0^1\int_0^1 \boldsymbol{\xi}_1(\hat{y}_c,\hat{z}_c)\cdot\mathbf{q}_0\,d\hat{y}d\hat{z} = \int_{\hat{E}} \hat{v}_1(\hat{x})\boldsymbol{\xi}_1(\hat{y}_c,\hat{z}_c)\cdot\mathbf{q}_0\,d\hat{x}d\hat{y}d\hat{z}.$$

Similar identities hold for the other terms on the right in (2.39). □

Lemma 2.4 *For any constant vector* $\mathbf{q}_0$ *on* E *and* $\mathbf{v}\in RT_0(E)$,

$$(K^{-1}\mathbf{q}_0,\mathbf{v})_{Q,E} = (\overline{K}_E^{-1}\mathbf{q}_0,\mathbf{v})_E. \tag{2.40}$$

Proof The proof is similar to the proof of Lemma 3.1 in [35]. By the definition (2.32) of the quadrature rule and the Piola transformation (2.12),

$$\begin{aligned}(K^{-1}\mathbf{q}_0,\mathbf{v})_{Q,E} &= \left(\frac{1}{J_E}DF_E^T(\hat{\mathbf{r}}_{c,\hat{E}})\overline{K}_E^{-1}DF_E\hat{\mathbf{q}}_0,\hat{\mathbf{v}}\right)_{\hat{Q},\hat{E}}\\ &= \left(DF_E^T(\hat{\mathbf{r}}_{c,\hat{E}})\overline{K}_E^{-1}\mathbf{q}_0,\hat{\mathbf{v}}\right)_{\hat{Q},\hat{E}} = \left(DF_E^T(\hat{\mathbf{r}}_{c,\hat{E}})\overline{K}_E^{-1}\mathbf{q}_0,\hat{\mathbf{v}}\right)_{\hat{E}}\\ &= \left(\overline{K}_E^{-1}\mathbf{q}_0,DF_E(\hat{\mathbf{r}}_{c,\hat{E}})\hat{\mathbf{v}}\right)_{\hat{E}} = \left(\overline{K}_E^{-1}\mathbf{q}_0,DF_E\hat{\mathbf{v}}\right)_{\hat{E}} = (\overline{K}_E^{-1}\mathbf{q}_0,\mathbf{v})_E,\end{aligned} \tag{2.41}$$

where we have used the fact that trapezoidal rule is exact for bilinear (trilinear) functions on $\hat{E}$, and (2.38). □

2.4 The multipoint flux mixed finite element method

The method is defined as follows: find $\mathbf{u}_h\in\mathbf{V}_h$ and $p_h\in W_h$ such that

$$(K^{-1}\mathbf{u}_h,\mathbf{v})_Q - (p_h,\nabla\cdot\mathbf{v}) = 0, \qquad \forall\mathbf{v}\in\mathbf{V}_h \tag{2.42}$$
$$(\nabla\cdot\mathbf{u}_h,w) = (f,w), \qquad \forall w\in W_h \tag{2.43}$$

Following the terminology from [33,51], we call the method (2.42)–(2.43) a non-symmetric multipoint flux mixed finite element (MFMFE) method, due to its relation to the MPFA method and the non-symmetric quadrature rule (2.33).

For the solvability of this system, we require the bilinear form $(\cdot,\cdot)_Q$ to be coercive. This holds if the matrix $\mathbf{M}_c$ associated with $(\cdot,\cdot)_Q$ is positive definite, see (3.27) in Sect. 3.2.

Lemma 2.5 *If* (3.27) *holds, then the method* (2.42)–(2.43) *has a unique solution.*

Proof It is sufficient to show the uniqueness since (2.42)–(2.43) is a finite-dimensional square linear system. We let $f = 0$ and choose $\mathbf{v} = \mathbf{u}_h$ and $w = p_h$ to conclude that $(K^{-1}\mathbf{u}_h, \mathbf{u}_h)_{Q,\Omega_i} = 0$. Since (3.27) holds, the norm equivalence (3.28) implies that $\mathbf{u}_h = 0$. For $p_h \in W_h \subset L^2(\Omega)$, there exists $\mathbf{q} \in (H^1(\Omega))^d$ such that $\nabla \cdot \mathbf{q} = p_h$ [31,30]. Taking $\mathbf{v} = \Pi\mathbf{q}$ in (2.42) and using (2.20) implies that $p_h = 0$. □

2.5 Reduction to a cell-centered stencil

In this section we describe how the multipoint flux mixed finite element method reduces to a system for the pressure at the cell centers. Consider any interior vertex $\mathbf{r}_c$ that is shared by k elements $E_1, \ldots, E_k$; see Fig. 4 for a two-dimensional example of five quadrilaterals sharing a vertex. Denote the faces that share the vertex by $e_1, \ldots, e_k$, and the corresponding velocity basis functions associated with the vertex by $\mathbf{v}_1, \ldots, \mathbf{v}_k$. Let the normal components of $\mathbf{u}_h$ on the edges be denoted by $u_1, \ldots, u_k$. Note that for clarity the normal velocities in Fig. 4 are drawn at a distance from the vertex.

Recall that the quadrature rule $(K^{-1}\cdot, \cdot)_Q$ decouples the basis functions that do not share a vertex (see (2.34)). Setting $\mathbf{v}_1$ in (2.42) leads to coupling of u_1 only with u_2 and u_5. Similarly, u_2 is coupled only with u_1 and u_3, etc. Thus, the five equations obtained by taking $\mathbf{v} = \mathbf{v}_1, \ldots, \mathbf{v}_5$ form a linear system for $u_1, \ldots, u_5$.

We derive the local linear system for the example in Fig. 4. Without loss of generality, assume that edges e_1 and e_3 are mapped to horizontal reference edges, edges e_2 and e_4 are mapped to vertical reference edges, e_5 in E_1 is mapped to a vertical edge and e_5 in E_5 is mapped to a horizontal reference edge.

Taking $\mathbf{v} = \mathbf{v}_3$ in (2.42) gives

$$(K^{-1}\mathbf{u}_h, \mathbf{v}_3)_Q = (K^{-1}\mathbf{u}_h, \mathbf{v}_3)_{Q,E_3} + (K^{-1}\mathbf{u}_h, \mathbf{v}_3)_{Q,E_4}. \tag{2.44}$$

By applying the quadrature rule (2.32), we have

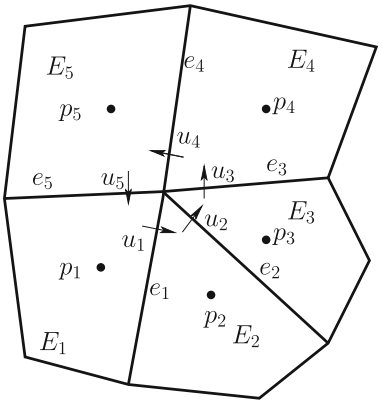

Fig. 4 Five quadrilaterals sharing a vertex and associated degrees of freedom

$$
\begin{aligned}
(K^{-1}\mathbf{u}_h, \mathbf{v}_3)_{Q,E_3} &= (\widetilde{\mathcal{M}}_{E_3}\hat{\mathbf{u}}_h, \hat{\mathbf{v}}_3)_{\hat{Q},\hat{E}} \\
&= u_2(\widetilde{\mathcal{M}}_{E_3}\hat{\mathbf{v}}_2, \hat{\mathbf{v}}_3)_{\hat{Q},\hat{E}} + u_3(\widetilde{\mathcal{M}}_{E_3}\hat{\mathbf{v}}_3, \hat{\mathbf{v}}_3)_{\hat{Q},\hat{E}} \\
&= \frac{1}{4}\left(-\widetilde{\mathcal{M}}^{12}_{E_3}|e_2|u_2 + \widetilde{\mathcal{M}}^{11}_{E_3}|e_3|u_3\right)|e_3|, \qquad (2.45)
\end{aligned}
$$

where we have used (2.15) in the last equality. Note that the components of $\widetilde{\mathcal{M}}_{E_3}$ are evaluated at the vertex. Similarly, the second term on the right of (2.44) can be written as

$$
(K^{-1}\mathbf{u}_h, \mathbf{v}_3)_{Q,E_4} = \frac{1}{4}\left(\widetilde{\mathcal{M}}^{11}_{E_4}|e|_3u_3 - \widetilde{\mathcal{M}}^{12}_{E_4}|e|_4u_4\right)|e_3|. \qquad (2.46)
$$

For the second term on the left of (2.42), we write

$$
\begin{aligned}
(p_h, \nabla\cdot\mathbf{v}_3) &= (p_h, \nabla\cdot\mathbf{v}_3)_{E_3} + (p_h, \nabla\cdot\mathbf{v}_3)_{E_4} \\
&= \langle p_h, \mathbf{v}_3\cdot\mathbf{n}_{E_3}\rangle_{e_3} + \langle p_h, \mathbf{v}_3\cdot\mathbf{n}_{E_4}\rangle_{e_3} \\
&= \langle \hat{p}_h, \hat{\mathbf{v}}_3\cdot\hat{\mathbf{n}}_{E_3}\rangle_{\hat{e}_3} + \langle \hat{p}_h, \hat{\mathbf{v}}_3\cdot\hat{\mathbf{n}}_{E_4}\rangle_{\hat{e}_3} = \frac{1}{2}(p_3 - p_4)|e_3|. \qquad (2.47)
\end{aligned}
$$

In the last equality we used the fact that trapezoidal rule is exact for the integrals on $\hat{e}_3$ since $\hat{p}_h$ is constant and $\hat{\mathbf{v}}_3\cdot\hat{\mathbf{n}}$ is linear (or bilinear for 3D elements). The above results gives the equation associated with test function $\mathbf{v}_3$ as:

$$
-\frac{1}{2}\widetilde{\mathcal{M}}^{12}_{E_3}|e_2|u_2 + \left(\frac{1}{2}\widetilde{\mathcal{M}}^{11}_{E_3} + \frac{1}{2}\widetilde{\mathcal{M}}^{11}_{E_4}\right)|e_3|u_3 - \frac{1}{2}\widetilde{\mathcal{M}}^{12}_{E_4}|e_4|u_4 = p_3 - p_4.
$$

Similarly we derive the other four equations of the local system and write the system as

$$
\mathbf{A}\widetilde{\mathbf{M}}_c\mathbf{A}\begin{pmatrix} u_1 \\ u_2 \\ u_3 \\ u_4 \\ u_5 \end{pmatrix} = \mathbf{A}\begin{pmatrix} 2p_1 - 2p_2 \\ 2p_2 - 2p_3 \\ 2p_3 - 2p_4 \\ 2p_4 - 2p_5 \\ 2p_5 - 2p_1 \end{pmatrix}, \qquad (2.48)
$$

where $\mathbf{A} = \mathrm{diag}(|e_1|, |e_2|, |e_3|, |e_4|, |e_5|)$ and

$$
\widetilde{\mathbf{M}}_c = \begin{pmatrix}
\widetilde{\mathcal{M}}^{11}_{E_1} + \widetilde{\mathcal{M}}^{11}_{E_2} & -\widetilde{\mathcal{M}}^{12}_{E_2} & & & -\widetilde{\mathcal{M}}^{12}_{E_1} \\
-\widetilde{\mathcal{M}}^{21}_{E_2} & \widetilde{\mathcal{M}}^{22}_{E_2} + \widetilde{\mathcal{M}}^{22}_{E_3} & -\widetilde{\mathcal{M}}^{21}_{E_3} & & \\
 & -\widetilde{\mathcal{M}}^{12}_{E_3} & \widetilde{\mathcal{M}}^{11}_{E_3} + \widetilde{\mathcal{M}}^{11}_{E_4} & -\widetilde{\mathcal{M}}^{12}_{E_4} & \\
 & & -\widetilde{\mathcal{M}}^{21}_{E_4} & \widetilde{\mathcal{M}}^{22}_{E_4} + \widetilde{\mathcal{M}}^{22}_{E_5} & -\widetilde{\mathcal{M}}^{21}_{E_5} \\
-\widetilde{\mathcal{M}}^{21}_{E_1} & & & -\widetilde{\mathcal{M}}^{12}_{E_5} & \widetilde{\mathcal{M}}^{11}_{E_5} + \widetilde{\mathcal{M}}^{22}_{E_1}
\end{pmatrix}. \qquad (2.49)
$$

Let $\mathbf{M}_c = \mathbf{A}\widetilde{\mathbf{M}}_c\mathbf{A}$. On general quadrilateral and hexahedral elements, $\mathbf{M}_c$ is not symmetric unless the meshes are parallelograms and parallelepipeds. The stability condition (3.27) ensures the solvability of this local system.

Let $\mathbf{M}$ be the matrix induced by the bilinear form $(K^{-1}\cdot,\cdot)_Q$. Clearly $\mathbf{M}$ is block-diagonal with each block $\mathbf{M}_c$ associated with a corner point c. The size of $\mathbf{M}_c$ is $n_c \times n_c$, where n_c is the number of faces (or edges in 2D) that share the vertex point c. The solution of the local $n_c \times n_c$ linear system allows for the normal component of velocities $u_i, i = 1, \ldots, n_c$ to be expressed in term of the pressure degrees of freedom $p_i, i = 1, \ldots N_c$ at the cell centers, where N_c is the number of elements that share the vertex c.

The discrete mass conservation equation (2.43) reads, taking $w = 1$ and using (2.14),

$$(\nabla \cdot \mathbf{u}_h, 1)_E = \sum_{e\in\partial E} \langle \mathbf{u}_h \cdot \mathbf{n}_e, 1\rangle_e = \sum_{\hat{e}\in\partial \hat{E}} \langle \hat{\mathbf{u}}_h \cdot \hat{\mathbf{n}}_{\hat{e}}, 1\rangle_{\hat{e}}, \tag{2.50}$$

where $\hat{\mathbf{u}}_h \cdot \hat{\mathbf{n}}_{\hat{e}}$ is linear (or bilinear) on the edge (or face) $\hat{e}$. Applying the trapezoidal rule for the quantity $\langle \hat{\mathbf{u}}_h \cdot \hat{\mathbf{n}}_{\hat{e}}, 1\rangle_{\hat{e}}$ is exact and gives a linear combination of the normal components of the velocities defined at the vertices of E. Then, substituting u_i from (2.48) into (2.50) gives a cell-centered stencil for the pressures. The pressure in each element E is coupled only with the pressures in elements that share a vertex with E. This gives a 9-point or a 27-point stencil on logically rectangular or cuboid grids, respectively.

3 Convergence of the velocity

In the error analysis, we will make use of the following auxiliary lemmas on general quadrilateral and hexahedral elements.

3.1 Auxiliary results

Lemma 3.6 ([33]) *For any element $E \in \mathcal{T}_h$,*

$$\|\mathbf{q}\|_{j,E} \lesssim h^{-1}\|\mathbf{q}\|_{j-1,E}, \quad j = 1, 2, \quad \forall \mathbf{q} \in \mathbf{V}_h(E). \tag{3.1}$$

The following are bounds on the Jacobian matrix terms that appear in the Piola transformation (2.12).

Lemma 3.7 *For a general quadrilateral and hexahedral element $E \in \mathcal{T}_h$,*

$$\left|\frac{1}{J_E} DF_E\right|_{0,\infty,E} \lesssim h^{1-d}, \tag{3.2}$$

$$|J_E DF_E^{-1}|_{j,\infty,\hat{E}} \lesssim h^{d-1}, \quad j = 0, 1. \tag{3.3}$$

Proof The proof for general hexahedra can be found in [33]. The proof for general quadrilaterals is similar. □

Remark 3.2 Better bounds can be obtained under a certain restriction on the element geometry. A quadrilateral in 2D or a hexahedral face in 3D with vertices $\mathbf{r}_1$, $\mathbf{r}_2$, $\mathbf{r}_3$, and $\mathbf{r}_4$ (numbered counter clockwise) is called an h^2-parallelogram if

$$|\mathbf{r}_{34} - \mathbf{r}_{21}|_{\mathbb{R}^d} \lesssim h^2.$$

A hexahedron is called an h^2-parallelepiped when all of its faces are h^2-parallelograms. For h^2-parallelograms and h^2-parallelepipeds, one order higher estimate holds for the one-seminorm; namely, $|J_E DF_E^{-1}|_{1,\infty,\hat{E}} \lesssim h^d$ (see [51,33]), as compared to (3.3) for general quadrilateral and hexahedral elements.

Lemma 3.8 *For any element $E \in \mathcal{T}_h$,*

$$\|\hat{\mathbf{q}}\|_{\hat{E}} \eqsim h^{-1+d/2}\|\mathbf{q}\|_E, \quad \forall \mathbf{q} \in (L^2(E))^d, \tag{3.4}$$

$$|\hat{\mathbf{q}}|_{1,\hat{E}} \lesssim (h^{-1+d/2}\|\mathbf{q}\|_E + h^{d/2}|\mathbf{q}|_{1,E}), \quad \forall \mathbf{q} \in (H^1(E))^d. \tag{3.5}$$

Proof Let $\tilde{\mathbf{q}}(\hat{\mathbf{x}}) = \mathbf{q} \circ F(\hat{\mathbf{x}})$. By the standard scaling argument [21] and the shape regularity of mesh,

$$|\tilde{\mathbf{q}}|_{j,\hat{E}} \eqsim h^{j-d/2}|\mathbf{q}|_{j,E}, \quad j = 0, 1. \tag{3.6}$$

The definition of the Piola transformation (2.12) implies,

$$\hat{\mathbf{q}}(\hat{\mathbf{x}}) = J_E DF_E^{-1}\tilde{\mathbf{q}}(\hat{\mathbf{x}}). \tag{3.7}$$

Then, by (3.3) and (3.6),

$$\|\hat{\mathbf{q}}\|_{\hat{E}} \leq |J_E DF_E^{-1}|_{0,\infty,\hat{E}}\|\tilde{\mathbf{q}}\|_{\hat{E}} \lesssim h^{d-1}h^{-d/2}\|\mathbf{q}\|_E = h^{-1+d/2}\|\mathbf{q}\|_E. \tag{3.8}$$

Similarly, using (3.2), one can show

$$\|\mathbf{q}\|_E \lesssim h^{1-d/2}\|\hat{\mathbf{q}}\|_{\hat{E}}. \tag{3.9}$$

Next, using (3.7), (3.3), and (3.6), we get

$$\begin{aligned} |\hat{\mathbf{q}}|_{1,\hat{E}} &\lesssim |J_E DF_E^{-1}|_{1,\infty,\hat{E}}\|\tilde{\mathbf{q}}\|_{\hat{E}} + |J_E DF_E^{-1}|_{0,\infty,\hat{E}}|\tilde{\mathbf{q}}|_{1,\hat{E}} \\ &\lesssim h^{d-1}h^{-d/2}\|\mathbf{q}\|_E + h^{d-1}h^{1-d/2}|\mathbf{q}|_{1,E} \\ &= h^{-1+d/2}\|\mathbf{q}\|_E + h^{d/2}|\mathbf{q}|_{1,E}. \end{aligned} \tag{3.10}$$

This gives (3.5). □

Lemma 3.9 *The following trace inequality holds:*

$$\|\mathbf{v}\cdot\mathbf{n}\|_{\partial E} \eqsim h^{-1/2}\|\mathbf{v}\|_E \quad \forall\, \mathbf{v}\in\mathbf{V}_h, \tag{3.11}$$

Proof First, note that (2.8) implies that $J_e \eqsim h^{d-1}$. Now, (3.11) follows from (2.15), the norm equivalence on the reference element $\hat{E}$, $\|\hat{\mathbf{v}}\cdot\hat{\mathbf{n}}\|_{\partial\hat{E}} \eqsim \|\hat{\mathbf{v}}\|_{\hat{E}}$, and the scaling estimate (3.4). □

Lemma 3.10 *The following estimates hold for all* $\mathbf{q}\in(H^1(E))^d$*:*

$$\|\Pi_R\mathbf{q}\|_E + \|\Pi\mathbf{q}\|_E \lesssim \|\mathbf{q}\|_E + h|\mathbf{q}|_{1,E}, \tag{3.12}$$

$$\|\nabla\cdot\Pi_R\mathbf{q}\|_E + \|\nabla\cdot\Pi\mathbf{q}\|_E \lesssim \|\nabla\cdot\mathbf{q}\|_E. \tag{3.13}$$

Proof We present the proof for Π_R. The proof for Π is similar. First, note that

$$\|\hat{\Pi}_R\hat{\mathbf{q}}\|_{\hat{E}} \lesssim \|\hat{\mathbf{q}}\|_{\hat{E}} + \|\hat{\Pi}_R\hat{\mathbf{q}}-\hat{\mathbf{q}}\|_{\hat{E}} \lesssim \|\hat{\mathbf{q}}\|_{\hat{E}} + |\hat{\mathbf{q}}|_{1,\hat{E}} \lesssim \|\hat{\mathbf{q}}\|_{1,\hat{E}}, \tag{3.14}$$

where we have used the Bramble–Hilbert lemma in the second inequality. Now, using (3.4), we have

$$\begin{aligned}\|\Pi_R\mathbf{q}\|_E &\lesssim h^{1-d/2}\|\hat{\Pi}_R\hat{\mathbf{q}}\|_{\hat{E}} \lesssim h^{1-d/2}\|\hat{\mathbf{q}}\|_{1,E}\\ &\lesssim h^{1-d/2}(h^{-1+d/2}\|\mathbf{q}\|_E + h^{d/2}|\mathbf{q}|_{1,E}) = \|\mathbf{q}\|_E + h|\mathbf{q}|_{1,E},\end{aligned} \tag{3.15}$$

using (3.5) in the last inequality. This gives (3.12). To show (3.13) we write, using (2.16) and (2.8),

$$\|\nabla\cdot\Pi_R\mathbf{q}\|_E \lesssim h_E^{-d/2}\|\hat{\nabla}\cdot\hat{\Pi}_R\hat{\mathbf{q}}\|_{\hat{E}} \le h_E^{-d/2}\|\hat{\nabla}\cdot\hat{\mathbf{q}}\|_{\hat{E}} \lesssim \|\nabla\cdot\mathbf{q}\|_E,$$

where we have used that $\hat{\nabla}\cdot\hat{\Pi}_R\hat{\mathbf{q}}$ is the $L^2(\hat{E})$-projection of $\hat{\nabla}\cdot\hat{\mathbf{q}}$. This completes the proof of (3.13). □

The next lemmas establish important properties of the mixed interpolant of constant (in 3D) and linear (in 2D) vectors in a physical element.

Lemma 3.11 *In the case of hexahedra, for any constant vector* $\mathbf{q}_0$ *on* E*,*

$$\forall\, e\subset\partial E, \quad \Pi\mathbf{q}_0\cdot\mathbf{n}_e = \mathbf{q}_0\cdot\mathbf{n}_e. \tag{3.16}$$

Proof The Piola transformation gives $\hat{\mathbf{q}}_0 = J_E DF_E^{-1}\mathbf{q}_0$ with $J_E DF_E^{-1} = C_E^T$, where C_E is the cofactor matrix of DF_E. Then

$$\hat{\mathbf{q}}_0\cdot\hat{\mathbf{n}}_{\hat{e}} = C_E^T\mathbf{q}_0\cdot\hat{\mathbf{n}}_{\hat{e}} = C_E\hat{\mathbf{n}}_{\hat{e}}\cdot\mathbf{q}_0.$$

It is easy to check by direct computation that

$$C_E = [\mathbf{c}_1,\mathbf{c}_2,\mathbf{c}_3], \quad \mathbf{c}_1\in(P_{2,1,1}(E))^3,\ \mathbf{c}_2\in(P_{1,2,1}(E))^3,\ \mathbf{c}_3\in(P_{1,1,2}(E))^3,$$

where $P_{\alpha_1,\alpha_2,\alpha_3}$ is the space of tensor-product polynomials of degree at most α_i in variable x_i, $i = 1, 2, 3$. A closer inspection shows that $C_E\hat{\mathbf{n}}_{\hat{e}} \in P_1(\hat{e})^3$. For example on the face ($\hat{x} = 0$) of the reference element $\hat{E}$, it is easy to calculate using (2.3)

$$C_E\hat{\mathbf{n}}_{\hat{e}} = -\begin{bmatrix} (c_2 + g_2\hat{z})(d_3 + g_3\hat{y}) - (d_2 + g_2\hat{y})(c_3 + g_3\hat{z}) \\ (d_1 + g_1\hat{y})(c_3 + g_3\hat{z}) - (c_1 + g_1\hat{z})(d_3 + g_3\hat{y}) \\ (c_1 + g_1\hat{z})(d_2 + g_2\hat{y}) - (d_1 + g_1\hat{y})(c_2 + g_2\hat{z}) \end{bmatrix},$$

where the constant vectors are $[c_1\ c_2\ c_3]^T = \mathbf{r}_{41}$, $[d_1\ d_2\ d_3]^T = \mathbf{r}_{51}$, and $[g_1\ g_2\ g_3]^T = \mathbf{r}_{85} - \mathbf{r}_{21}$. This gives $C_E\hat{\mathbf{n}}_{\hat{e}} \cdot \mathbf{q}_0 \in P_1(\hat{e})$, implying that $\hat{\mathbf{q}}_0 \cdot \hat{\mathbf{n}}_{\hat{e}} \in P_1(\hat{e}) \subset \hat{\mathbf{V}}(\hat{E}) \cdot \hat{\mathbf{n}}_{\hat{e}}$.

Now, (2.18) implies that $\hat{\Pi}\hat{\mathbf{q}}_0 \cdot \hat{\mathbf{n}}_{\hat{e}} = \hat{\mathbf{q}}_0 \cdot \hat{\mathbf{n}}_{\hat{e}}$ and the proof is completed by using (2.15). □

Lemma 3.12 *In the case of quadrilaterals, for any linear vector* $\mathbf{q}_1$ *on* E,

$$\forall\, e \subset \partial E, \quad \Pi\mathbf{q}_1 \cdot \mathbf{n}_e = \mathbf{q}_1 \cdot \mathbf{n}_e. \tag{3.17}$$

Proof Let $\hat{\mathbf{q}}_1 = J_E DF_E^{-1}\mathbf{q}_1$. Due to (2.15), it is enough to show on any edge $\hat{e}$,

$$\hat{\Pi}\hat{\mathbf{q}}_1 \cdot \hat{\mathbf{n}}_{\hat{e}} = \hat{\mathbf{q}}_1 \cdot \hat{\mathbf{n}}_{\hat{e}}. \tag{3.18}$$

Let $\mathbf{q}_1 = [a_1 + b_1x + c_1y \quad a_2 + b_2x + c_2y]^T$ and the constant normal vector $\mathbf{n}_e = [d_1\ d_2]^T$. By (2.15)

$$\hat{\mathbf{q}}_1 \cdot \hat{\mathbf{n}}_{\hat{e}} = |e|\mathbf{q}_1 \cdot \mathbf{n}_e = |e| \sum_{i=1}^{2} (a_i + b_ix + c_iy)d_i. \tag{3.19}$$

Then by (2.4), we have $\hat{\mathbf{q}}_1 \cdot \hat{\mathbf{n}}_{\hat{e}} \in P_1(\hat{e})$. Now, (2.18) implies (3.18). □

Remark 3.3 The above result in 3D relies on the key property that the Piola image of a constant vector on a physical element has a linear normal component in the reference element, which belongs to the BDDF_1 space and the enhanced BDDF_1 space. This property does not hold for the RT_0 interpolant, which has a constant normal component on the reference element.

In the analysis, we will use the following well-known estimates [13]. There exists $q^1 \in P_1(E)$ such that

$$\|p - q^1\|_{j,E} \lesssim h^{2-j}\|p\|_{2,E}, \quad j = 0, 1, \tag{3.20}$$

and

$$\|p - q^1\|_E \lesssim h\|p\|_{1,E}. \tag{3.21}$$

Using the trace inequality for Lipschitz domains [6,9],

$$\forall\, e \in \partial E, \quad \|\phi\|_e \lesssim h^{-1/2}\|\phi\|_E + h^{1/2}|\phi|_{1,E}, \quad \forall \phi \in H^1(E), \tag{3.22}$$

we have the interpolation estimate on e:

$$\|p - q^1\|_e \lesssim h^{3/2}|p|_{2,E}. \tag{3.23}$$

We also have [21]

$$\|K - \overline{K}_E\|_E \lesssim h\|K\|_{1,E}. \tag{3.24}$$

3.2 Coercivity of the velocity bilinear form

For the analysis of non-symmetric MFMFE method we require some properties of the bilinear form $(K^{-1}\cdot, \cdot)_Q$ defined on the space $\mathbf{V}_h$. Note that

$$(K^{-1}\mathbf{q}, \mathbf{v})_Q = \sum_{E\in\mathcal{T}_h} (K^{-1}\mathbf{q}, \mathbf{v})_{Q,E} = \sum_{c\in\mathcal{C}_h} \mathbf{v}_c^T \mathbf{M}_c \mathbf{q}_c = \mathbf{v}_\Omega^T \mathbf{M}\mathbf{q}_\Omega, \tag{3.25}$$

where $\mathcal{C}_h$ denotes the set of corner or vertex points in $\mathcal{T}_h$, $\mathbf{v}_c := \{(\mathbf{v}\cdot\mathbf{n}_e)(\mathbf{x}_c)\}_{e=1}^{n_c}$, $\mathbf{x}_c$ is the coordinate vector of point c, and n_c is the number of faces (or edges in 2D) that share the vertex point c. An example of the $n_c \times n_c$ matrix $\mathbf{M}_c$ is given in (2.49). In the above, $\mathbf{v}_\Omega$ is the global vector of values of the normal trace degrees of freedom of $\mathbf{v}$ in $\mathbf{V}_h$ and $\mathbf{M}$ is the block-diagonal matrix with blocks $\mathbf{M}_c$, $c \in \mathcal{C}_h$. From (2.30) and (2.8) one can see that

$$\|\mathbf{M}_c\|_{0,\infty,\hat{E}} \eqsim h^d \|K^{-1}\|_{0,\infty,E}. \tag{3.26}$$

Lemma 3.13 *Assume that $\mathbf{M}_c$ is uniformly positive definite for all $c \in \mathcal{C}_h$:*

$$h^d \boldsymbol{\xi}^T \boldsymbol{\xi} \lesssim \boldsymbol{\xi}^T \mathbf{M}_c \boldsymbol{\xi}, \quad \forall \boldsymbol{\xi} \in \mathbb{R}^{n_c}. \tag{3.27}$$

Then the bilinear form $(K^{-1}\cdot, \cdot)_Q$ is coercive in $\mathbf{V}_h$ and induces a norm in $\mathbf{V}_h$ equivalent to the L^2-norm:

$$(K^{-1}\mathbf{v}, \mathbf{v})_Q \eqsim \|\mathbf{v}\|^2, \quad \forall\, \mathbf{v} \in \mathbf{V}_h. \tag{3.28}$$

If in addition

$$\boldsymbol{\xi}^T \mathbf{M}_c^T \mathbf{M}_c \boldsymbol{\xi} \lesssim h^{2d} \boldsymbol{\xi}^T \boldsymbol{\xi}, \quad \forall\, \boldsymbol{\xi} \in \mathbb{R}^{n_c}, \tag{3.29}$$

then the following Cauchy–Schwarz type inequality holds:

$$(K^{-1}\mathbf{q}, \mathbf{v})_Q \lesssim \|\mathbf{q}\|\|\mathbf{v}\| \quad \forall \mathbf{q}, \mathbf{v} \in \mathbf{V}_h, \tag{3.30}$$

Proof Let $\mathbf{v} \in \mathbf{V}_h$. Using the shape regularity of $\mathcal{T}_h$, it is easy to check by direct calculation that for all $E \in \mathcal{T}_h$

$$\|\mathbf{v}\|_E^2 \lesssim h^d \mathbf{v}_E^T \mathbf{v}_E,$$

where $\mathbf{v}_E$ is the vector of values of the degrees of freedom of $\mathbf{v}$ in E. We then have

$$\|\mathbf{v}\|^2 \lesssim \sum_{E\in\mathcal{T}_h} h^d \mathbf{v}_E^T \mathbf{v}_E \lesssim \sum_{c\in\mathcal{C}_h} h^d \mathbf{v}_c^T \mathbf{v}_c \lesssim \sum_{c\in\mathcal{C}_h} \mathbf{v}_c^T \mathbf{M}_c \mathbf{v}_c = (K^{-1}\mathbf{v}, \mathbf{v})_Q,$$

where we have used (3.27) and (3.25). This implies that $\mathbf{M}^s = \frac{1}{2}(\mathbf{M} + \mathbf{M}^T)$ is symmetric and positive definite and that $(K^{-1}\mathbf{v}, \mathbf{v})_Q = \mathbf{v}_\Omega^T \mathbf{M} \mathbf{v}_\Omega = \mathbf{v}_\Omega^T \mathbf{M}^s \mathbf{v}_\Omega$ is a norm. The equivalence to $\|\mathbf{v}\|$ follows from (3.26). If (3.29) holds, then (3.30) follows from the Cauchy–Schwarz inequality for the norm induced by the matrix $\mathbf{M}^T\mathbf{M}$. □

In practice, we can verify the assumptions (3.27) and (3.29) by considering only the local $d \times d$ matrix associated with a vertex of an element E. In particular, $\mathbf{M} = \sum_{E\in\mathcal{T}_h} \mathbf{M}_E$, where $\mathbf{M}_E$ is a block diagonal matrix with 2^d blocks of size $d \times d$ corresponding to the vertices of E. For any vertex c of E, denote the associated $d \times d$ matrix by $\mathbf{M}_E^c$. It is easy to check that

$$h^d \boldsymbol{\eta}^T \boldsymbol{\eta} \lesssim \boldsymbol{\eta}^T \mathbf{M}_E^c \boldsymbol{\eta} \quad \forall\, \boldsymbol{\eta} \in \mathbb{R}^d \tag{3.31}$$

and

$$\boldsymbol{\eta}^T (\mathbf{M}_E^c)^T \mathbf{M}_E^c \boldsymbol{\eta} \lesssim h^{2d} \boldsymbol{\eta}^T \boldsymbol{\eta}, \quad \forall\, \boldsymbol{\eta} \in \mathbb{R}^d \tag{3.32}$$

imply (3.27) and (3.29), respectively.

Conditions (3.31) and (3.32) impose restrictions on the element geometry and the anisotropy of the permeability tensor K. We refer readers to [35,37] for discussions on these conditions.

For the permeability tensor K, we will use the following notation. Let $W_{\mathcal{T}_h}^{\alpha,\infty}$ consist of functions ϕ such that $\phi|_E \in W^{\alpha,\infty}(E)$ for all $E \in \mathcal{T}_h$. Here α is an integer. Let $|||\phi|||_{\alpha,\infty} = \max_{E\in\mathcal{T}_h} \|\phi\|_{\alpha,\infty,E}$.

3.3 Convergence of the velocity to the interpolant of the solution

We are now ready to establish first order convergence of the computed velocity to the MFE interpolant of the true solution.

Theorem 3.1 *Let $K \in W_{\mathcal{T}_h}^{1,\infty}(\Omega)$ and $K^{-1} \in W^{0,\infty}(\Omega)$. If (3.27) and (3.29) hold, then the velocity $\mathbf{u}_h$ of the non-symmetric MFMFE method (2.42)–(2.43) satisfies*

$$\|\Pi\mathbf{u} - \mathbf{u}_h\| \lesssim h(|\mathbf{u}|_1 + \|p\|_2), \tag{3.33}$$

Proof Let $\mathbf{v} = \Pi\mathbf{u} - \mathbf{u}_h$, and note that (1.2), (2.43), and (2.20) imply that

$$(\nabla \cdot \mathbf{v}, w) = 0 \quad \forall\, w \in W_h.$$

Taking $w \in W_h$ such that $w|_E = J_E \nabla \cdot \mathbf{v}$ for all $E \in \mathcal{T}_h$ implies that $\nabla \cdot \mathbf{v} = 0$. Then from (2.42) we have

$$\begin{aligned}
&\left(K^{-1}(\Pi\mathbf{u} - \mathbf{u}_h), \Pi\mathbf{u} - \mathbf{u}_h\right)_Q \\
&= \left(K^{-1}\Pi\mathbf{u}, \mathbf{v}\right)_Q - (p_h, \nabla \cdot \mathbf{v}) = \left(K^{-1}\Pi\mathbf{u}, \mathbf{v}\right)_Q \\
&= \sum_{E\in\mathcal{T}_h} \left(K^{-1}\Pi(\mathbf{u} + \overline{K}_E \nabla q^1), \mathbf{v}\right)_{Q,E} - \sum_{E\in\mathcal{T}_h} \left(K^{-1}\Pi(\overline{K}_E \nabla q^1), \mathbf{v}\right)_{Q,E} \\
&\equiv I_1 + I_2, \qquad (3.34)
\end{aligned}$$

where q^1 is defined in (3.20). The term I_2 in (3.34) can be manipulated as

$$\begin{aligned}
\left(K^{-1}\Pi(\overline{K}_E \nabla q^1), \mathbf{v}\right)_{Q,E} &= \left(K^{-1}\overline{K}_E \nabla q^1, \mathbf{v}\right)_{Q,E} \\
&= \left(K^{-1}\overline{K}_E \nabla q^1, \Pi_R \mathbf{v}\right)_{Q,E} = \left(\nabla q^1, \Pi_R \mathbf{v}\right)_E, \qquad (3.35)
\end{aligned}$$

using (3.16), (2.36) and (2.40). Note that

$$\sum_{E\in\mathcal{T}_h} (\nabla p, \Pi_R \mathbf{v})_E = (\nabla p, \Pi_R \mathbf{v}) = (p, \nabla \cdot \Pi_R \mathbf{v}) = (p, \nabla \cdot \mathbf{v}) = 0,$$

using (2.25) and the fact that $p = 0$ on $\partial\Omega$. Then I_2 can be further written as

$$\begin{aligned}
I_2 &= \sum_{E\in\mathcal{T}_h} (\nabla(p - q^1), \Pi_R \mathbf{v})_E \lesssim \sum_{E\in\mathcal{T}_h} \|\nabla(p - q^1)\|_E \|\Pi_R \mathbf{v}\|_E \\
&\lesssim \sum_{E\in\mathcal{T}_h} h\|p\|_{2,E}(\|\mathbf{v}\|_E + h|\mathbf{v}|_{1,E}) \lesssim h\|p\|_2\|\mathbf{v}\|, \qquad (3.36)
\end{aligned}$$

where we have used (3.20), (3.12), and (3.1). To bound I_1, we write

$$\begin{aligned}
(K^{-1}\Pi(\mathbf{u} + \overline{K}_E \nabla q^1), \mathbf{v})_{Q,E} &\lesssim \|\Pi(\mathbf{u} + \overline{K}_E \nabla q^1)\|_E \|\mathbf{v}\|_E \\
&\lesssim (\|\mathbf{u} + \overline{K}_E \nabla q^1\|_E + h|\mathbf{u} + \overline{K}_E \nabla q^1|_{1,E})\|\mathbf{v}\|_E \\
&= (\|\mathbf{u} + \overline{K}_E \nabla q^1\|_E + h|\mathbf{u}|_{1,E})\|\mathbf{v}\|_E, \qquad (3.37)
\end{aligned}$$

using (3.30), (3.12), and the fact that $\overline{K}_E \nabla q^1$ is a constant vector. It remains to estimate $\|\mathbf{u} + \overline{K}_E \nabla q^1\|_E$. From (3.20) and (3.24), we have

$$\begin{aligned}
\|\mathbf{u} + \overline{K}_E \nabla q^1\|_E &\le \|(K - \overline{K}_E)\nabla p\|_E + \|\overline{K}_E \nabla(p - q^1)\|_E \\
&\lesssim h(\|\nabla p\|_E + \|p\|_{2,E}) \lesssim h\|p\|_{2,E}. \qquad (3.38)
\end{aligned}$$

A combination of (3.37) and(3.38) gives

$$|I_1| \lesssim h(\|p\|_2 + |\mathbf{u}|_1)\|\mathbf{v}\|. \qquad (3.39)$$

The proof is completed by combining (3.34), (3.36), (3.39), and (3.28). □

3.4 Convergence of the velocity on the element faces

In this section we show that the result from the previous section implies convergence of the computed normal velocity to the true normal velocity on the element faces. We introduce a norm for vectors in Ω based on the normal components on the faces of $\mathcal{T}_h$:

$$\|\mathbf{v}\|^2_{\mathcal{F}_h} := \sum_{E\in\mathcal{T}_h}\sum_{e\in\partial E}\frac{|E|}{|e|}\|\mathbf{v}\cdot\mathbf{n}_e\|^2_e, \tag{3.40}$$

where $|E|$ is the volume of E and $|e|$ is the area of e. This norm gives an appropriate scaling of size of $|\Omega|$ for a unit vector. The shape regularity assumption on the mesh implies that $|E|/|e| \eqsim h$, which gives

$$\|\mathbf{v}\|_{\mathcal{F}_h} \eqsim h^{1/2}\left(\sum_{E\in\mathcal{T}_h}\sum_{e\in\partial E}\|\mathbf{v}\cdot\mathbf{n}_e\|^2_e\right)^{1/2}. \tag{3.41}$$

The next result establishes approximation for the enhanced BDDF_1 interpolant in the norm $\|\cdot\|_{\mathcal{F}_h}$.

Lemma 3.14 *On hexahedra,*

$$\|(\mathbf{u}-\Pi\mathbf{u})\cdot\mathbf{n}_e\|_e \lesssim h^{1/2}|\mathbf{u}|_{1,E}, \tag{3.42}$$

and

$$\|\mathbf{u}-\Pi\mathbf{u}\|_{\mathcal{F}_h} \lesssim h|\mathbf{u}|_1. \tag{3.43}$$

On quadrilaterals,

$$\|(\mathbf{u}-\Pi\mathbf{u})\cdot\mathbf{n}_e\|_e \lesssim h^{j+1/2}|\mathbf{u}|_{j+1,E}, \quad j=0,1 \tag{3.44}$$

and

$$\|\mathbf{u}-\Pi\mathbf{u}\|_{\mathcal{F}_h} \lesssim h^{j+1}|\mathbf{u}|_{j+1}, \quad j=0,1. \tag{3.45}$$

Proof Let $\mathbf{q}$ be any constant vector on E in the case of hexahedra or a linear vector on E in the case of quadrilaterals. Lemma 3.11 and Lemma 3.12 imply that

$$\begin{aligned}\|(\mathbf{u}-\Pi\mathbf{u})\cdot\mathbf{n}_e\|_e &= \|(\mathbf{u}-\mathbf{q})\cdot\mathbf{n}_e - (\Pi\mathbf{u}-\Pi\mathbf{q})\cdot\mathbf{n}_e\|_e \\ &\le \|(\mathbf{u}-\mathbf{q})\cdot\mathbf{n}_e\|_e + \|\Pi(\mathbf{u}-\mathbf{q})\cdot\mathbf{n}_e\|_e. \end{aligned}\tag{3.46}$$

By the trace inequality (3.22), we have

$$\|(\mathbf{u}-\mathbf{q})\cdot\mathbf{n}_e\|_e \lesssim h^{-1/2}\|\mathbf{u}-\mathbf{q}\|_E + h^{1/2}|\mathbf{u}-\mathbf{q}|_{1,E}. \tag{3.47}$$

The trace inequality (3.11) implies that

$$\|\Pi(\mathbf{u}-\mathbf{q})\cdot\mathbf{n}_e\|_e \lesssim h^{-1/2}\|\Pi(\mathbf{u}-\mathbf{q})\|_E \lesssim h^{-1/2}\|\mathbf{u}-\mathbf{q}\|_E + h^{1/2}|\mathbf{u}-\mathbf{q}|_{1,E}, \tag{3.48}$$

where we have also used (3.12) in the last inequality. Taking $\mathbf{q}$ to be the L^2-projection of $\mathbf{u}$ into the space of constant vectors on E in the case of hexahedra or into the space of linear vectors in the case quadrilaterals in (3.46)–(3.48) yields (3.42) and (3.44). Inequalities (3.43) and (3.45) follow from (3.42) and (3.44), respectively, and (3.41). □

Remark 3.4 The above result for the enhanced BDDF_1 interpolant relies on Lemma 3.11. Therefore, due to Remark 3.3, similar approximation result also holds for the standard BDDF_1 interpolant, but it does not hold for the RT_0 interpolant.

Theorem 3.2 *Let $K \in W^{1,\infty}_{\mathcal{T}_h}(\Omega)$ and $K^{-1} \in W^{0,\infty}_{\mathcal{T}_h}(\Omega)$. If (3.27) and (3.29) hold, then the velocity $\mathbf{u}_h$ of the non-symmetric MFMFE method (2.42)–(2.43) satisfies*

$$\|\mathbf{u}-\mathbf{u}_h\|_{\mathcal{F}_h} \lesssim h(\|\mathbf{u}\|_1 + \|p\|_2). \tag{3.49}$$

Proof The triangle inequality gives

$$\begin{aligned}\|(\mathbf{u}-\mathbf{u}_h)\cdot\mathbf{n}_e\|_e &\le \|(\mathbf{u}-\Pi\mathbf{u})\cdot\mathbf{n}_e\|_e + \|(\Pi\mathbf{u}-\mathbf{u}_h)\cdot\mathbf{n}_e\|_e\\ &\lesssim h^{1/2}|\mathbf{u}|_{1,E} + h^{-1/2}\|\Pi\mathbf{u}-\mathbf{u}_h\|_E,\end{aligned}$$

where we have used (3.42) and (3.11) in the second inequality. The assertion of the theorem follows by combining the above inequality with (3.41) and (3.33). □

Remark 3.5 It is easy to see that the analysis presented in this section is valid also for the method (2.42)–(2.43) using the BDDF_1 space instead of the enhanced BDDF_1 space. Recall that the standard BDDF_1 MFE method does not converge on general hexahedra. Our results indicate that, while the quadrature rule $(\cdot,\cdot)_Q$ does not lead to a cell-centered finite difference system for the pressure in the case of the BDDF_1 space, it does lead to a method that gives a first order accurate fluxes on the hexahedral faces.

4 Convergence of the pressure

Lemma 4.15 *The spaces $\mathbf{V}_h^R \times W_h$ satisfy the inf–sup condition:*

$$\sup_{0\neq\mathbf{v}\in\mathbf{V}_h^R} \frac{(\nabla\cdot\mathbf{v}, w)}{\|\mathbf{v}\|_{\mathrm{div}}} \gtrsim \|w\|, \quad \forall w \in W_h. \tag{4.1}$$

Proof It is enough to show that $\forall w \in W_h$ there exists $\mathbf{v} \in \mathbf{V}_h^R$ such that

$$(\nabla \cdot \mathbf{v}, w) = \|w\|^2 \quad \text{and} \quad \|\mathbf{v}\|_{\text{div}} \lesssim \|w\|. \tag{4.2}$$

As noted in the proof of Lemma 2.5, for any $w \in W_h \subset L^2(\Omega)$, there exists $\mathbf{q} \in H^1(\Omega)$ such that [31,30]

$$\nabla \cdot \mathbf{q} = w \quad \text{and} \quad \|\mathbf{q}\|_1 \lesssim \|w\|, \tag{4.3}$$

Using (2.25), we have

$$(\nabla \cdot \Pi_R \mathbf{q}, w) = (\nabla \cdot \mathbf{q}, w) = \|w\|^2. \tag{4.4}$$

Furthermore, (3.12), (3.13), and (4.3) imply that

$$\|\Pi_R \mathbf{q}\|_{\text{div}} \lesssim \|\mathbf{q}\|_1 \lesssim \|w\|. \tag{4.5}$$

Now, (4.4) and (4.5) imply that $\mathbf{v} = \Pi_R \mathbf{q}$ satisfies (4.2), which completes the proof. □

Theorem 4.3 *Assume that* $K \in W^{1,\infty}_{\mathcal{T}_h}(\Omega)$, $K^{-1} \in W^{0,\infty}_{\mathcal{T}_h}(\Omega)$, *and that* (3.27) *and* (3.29) *hold. Then the pressure* p_h *of the non-symmetric MFMFE method* (2.42)–(2.43) *satisfies*

$$\|p - p_h\| \lesssim h(|\mathbf{u}|_1 + \|p\|_2). \tag{4.6}$$

Proof By Lemma 4.15, we have

$$\|Q_h p - p_h\| \lesssim \sup_{\mathbf{v} \in \mathbf{V}_h^R} \frac{(\nabla \cdot \mathbf{v}, Q_h p - p_h)}{\|\mathbf{v}\|_{\text{div}}}. \tag{4.7}$$

Using (2.27) and (2.42), the numerator can be written as

$$\begin{aligned}
(\nabla \cdot \mathbf{v}, Q_h p - p_h) &= (\nabla \cdot \mathbf{v}, p - p_h) = (\nabla \cdot \mathbf{v}, p - q^1) + (\nabla \cdot \mathbf{v}, q^1) - (\nabla \cdot \mathbf{v}, p_h) \\
&= (\nabla \cdot \mathbf{v}, p - q^1) + \sum_{E \in \mathcal{T}_h} \sum_{e \in \partial E} \langle q^1, \mathbf{v} \cdot \mathbf{n} \rangle_e + (K^{-1}(\Pi \mathbf{u} - \mathbf{u}_h), \mathbf{v})_Q \\
&\quad - \sum_{E \in \mathcal{T}_h} \left((K^{-1} \Pi \mathbf{u}, \mathbf{v})_{Q,E} + (\nabla q^1, \mathbf{v})_E \right) \\
&\equiv I_1 + I_2 + I_3 + I_4,
\end{aligned}$$

where q^1 is defined by (3.21). Term I_1 is estimated using (3.21):

$$|I_1| \lesssim h \|p\|_1 \|\nabla \cdot \mathbf{v}\|. \tag{4.8}$$

Using the continuity of p, (3.23), and (3.11), term I_2 can be written as

$$|I_2| = \left| \sum_{E\in\mathcal{T}_h} \sum_{e\in\partial E} \langle q^1 - p, \mathbf{v}\cdot\mathbf{n}\rangle_e \right| \le \sum_{E\in\mathcal{T}_h} \sum_{e\in\partial E} \|q^1 - p\|_e \|\mathbf{v}\cdot\mathbf{n}\|_e$$
$$\lesssim h^{3/2}|p|_2 h^{-1/2}\|\mathbf{v}\| = h|p|_2\|\mathbf{v}\|. \tag{4.9}$$

Using (3.30), term I_3 is estimated from Theorem 3.1 as:

$$|I_3| \lesssim h(|\mathbf{u}|_1 + \|p\|_2)\|\mathbf{v}\|. \tag{4.10}$$

Term I_4 can be written as

$$\begin{aligned} I_4 &= \sum_{E\in\mathcal{T}_h} \left((K^{-1}\Pi K\nabla p, \mathbf{v})_{Q,E} - (\nabla q^1, \mathbf{v})_E \right) \\ &= \sum_{E\in\mathcal{T}_h} \left(K^{-1}\Pi(K\nabla p - \overline{K}_E\nabla q^1), \mathbf{v} \right)_{Q,E} \\ &\quad + \sum_{E\in\mathcal{T}_h} \left((K^{-1}\Pi\overline{K}_E\nabla q^1, \mathbf{v})_{Q,E} - (\nabla q^1, \mathbf{v})_E \right) \\ &\equiv I_4^a + I_4^b \end{aligned} \tag{4.11}$$

Using (3.30) and (3.12), we estimate term I_4^a as

$$\begin{aligned} |I_4^a| &\lesssim \sum_{E\in\mathcal{T}_h} \|K^{-1}\Pi(K\nabla p - \overline{K}_E\nabla q^1)\|_E \|\mathbf{v}\|_E \\ &\lesssim \sum_{E\in\mathcal{T}_h} (\|K\nabla p - \overline{K}_E\nabla q^1\|_E + h|K\nabla p - \overline{K}_E\nabla q^1|_{1,E})\|\mathbf{v}\|_E \\ &\lesssim \sum_{E\in\mathcal{T}_h} (\|(K - \overline{K}_E)\nabla p\|_E + \|\overline{K}_E(\nabla p - \nabla q^1)\|_E + h|p|_{2,E})\|\mathbf{v}\|_E \\ &\lesssim h\|p\|_2\|\mathbf{v}\|, \end{aligned} \tag{4.12}$$

where we used (3.24) and (3.20) in the last inequality. Using (3.16) (or (3.17) for 2D) and Lemma 2.4, we have that

$$I_4^b = (K^{-1}\overline{K}_E\nabla q^1, \mathbf{v})_Q - (\nabla q^1, \mathbf{v}) = 0. \tag{4.13}$$

A combination of (4.7)–(4.13) and (2.28) completes the proof. □

Remark 4.6 Our error analysis also holds when the mean value of K^{-1} is used in the numerical quadrature rule (2.33) instead of the inverse of $\overline{K}$. Let us denote this quadrature rule by $(\cdot,\cdot)_{\widetilde{Q}}$:

$$(K^{-1}\mathbf{q},\mathbf{v})_{\widetilde{Q},E} \equiv \frac{1}{2^d}\sum_{i=1}^{2^d} J_E(\hat{\mathbf{r}}_i)(DF_E^{-1})^T(\mathbf{r}_i)DF_E^T(\hat{\mathbf{r}}_{c,\hat{E}})\overline{K_E^{-1}}\mathbf{q}(\mathbf{r}_i)\cdot\mathbf{v}(\mathbf{r}_i). \quad (4.14)$$

It is easy to see that Lemma 2.4 takes the form

$$(K^{-1}\mathbf{q}_0,\mathbf{v})_{\widetilde{Q},E} = (\overline{K_E^{-1}}\mathbf{q}_0,\mathbf{v})_E,$$

with $\overline{K}_E^{-1}$ being replaced by $\overline{K_E^{-1}}$. Using this identity, (3.35) becomes

$$\left(K^{-1}\overline{K}_E\nabla q^1,\Pi_R\mathbf{v}\right)_{\widetilde{Q},E} = \left(\nabla q^1,\Pi_R\mathbf{v}\right)_E + \left(\left(\overline{K_E^{-1}}-\overline{K}_E^{-1}\right)\overline{K}_E\nabla q^1,\Pi_R\mathbf{v}\right)_E,$$

and I_4^b in (4.13) becomes

$$I_4^b = (K^{-1}\overline{K}_E\nabla q^1,\mathbf{v})_{\widetilde{Q}} - (\nabla q^1,\mathbf{v}) = \left(\left(\overline{K_E^{-1}}-\overline{K}_E^{-1}\right)\overline{K}_E\nabla q^1,\mathbf{v}\right)_E.$$

Note that the extra terms are $\mathcal{O}(h)$, as they involve the difference between $\overline{K_E^{-1}}$ and $\overline{K}_E^{-1}$. Thus Theorems 3.1, 3.2, and 4.3 also hold for the quadrature rule (4.14).

5 Numerical experiments

In this section, we test both the symmetric and the non-symmetric MFMFE methods on h^2-parallelograms and h^2-parallelepipeds as well as on highly distorted quadrilaterals and hexahedra. The velocity error $\|\Pi\mathbf{u}-\mathbf{u}_h\|$ is approximated by the trapezoidal quadrature rule. The face error $\|\mathbf{u}-\mathbf{u}_h\|_{\mathcal{F}_h}$ is computed by the 3-point or 9-point Gaussian quadrature rules on edges or faces. The pressure error $\|p-p_h\|$ is approximated by the 9-point or 27-point Gauss quadrature rules on quadrilaterals and hexahedra. The discrete L^2 pressure error $|||p-p_h|||$ is computed by the midpoint quadrature rule: $|||p-p_h|||^2 \equiv \sum_{E\in\mathcal{T}_h}|E|(p-p_h)^2(m_e)$, where m_e is the center of mass of the element E. We also report convergence in the discrete flux error

$$|||\mathbf{u}-\mathbf{u}_h|||_{\mathcal{F}_h}^2 \equiv \sum_{E\in\mathcal{T}_h}\sum_{e\in\partial E}|E|\left(\frac{1}{|e|}\int_e \mathbf{u}\cdot\mathbf{n}_e - \frac{1}{|e|}\int_e \mathbf{u}_h\cdot\mathbf{n}_e\right)^2.$$

The resulting linear algebraic system is solved using the software HYPRE (high performance preconditioners) developed by researchers at Lawrence Livermore National Laboratory.[1]

[1] http://computation.llnl.gov/casc/hypre/software.html.

5.1 2D examples

We consider two types of meshes—smooth and non-smooth. The smooth mesh is a C^∞ map of a uniform mesh on the unit square. The map is defined as

$$x = \hat{x} + 0.06 \sin(2\pi \hat{x}) \sin(2\pi \hat{y}),$$
$$y = \hat{y} - 0.05 \sin(2\pi \hat{x}) \sin(2\pi \hat{y}).$$

The mesh is shown on the left in Fig. 5. It is easy to check that in this case the elements are h^2-parallelograms. The second mesh consists of highly distorted quadrilaterals generated by perturbing the uniform mesh points in a random direction by a distance of size $\mathcal{O}(h)$, see the right Fig. 5. The grids on the different levels of refinement are obtained by mapping or perturbing refinements of the uniform grid.

We consider problem (1.1)–(1.2) with a given analytical solution

$$p(x, y) = \sin(3\pi x)^2 \sin(3\pi y)^2,$$

and full permeability tensor

$$\mathbf{K} = \begin{pmatrix} 2 & 1.25 \\ 1.25 & 3 \end{pmatrix}.$$

The boundary conditions are of Dirichlet type.

We first test the convergence of $\|\mathbf{u} - \Pi\mathbf{u}\|_{\mathcal{F}_h}$. The results for $\mathbf{u} = -K\nabla p$, where p and K are defined above, are given in Table 1. We observe second order convergence on both the smooth grids and the rough grids, which confirms the theoretical results in Sect. 3.4. The slight variation in the convergence rate on the randomly perturbed grids is due to varying shape regularity constants on the different grid levels.

Next, we test the convergence of the MFMFE method. Table 2 shows the numerical results on h^2-parallelogram meshes. As the theory predicts for the symmetric

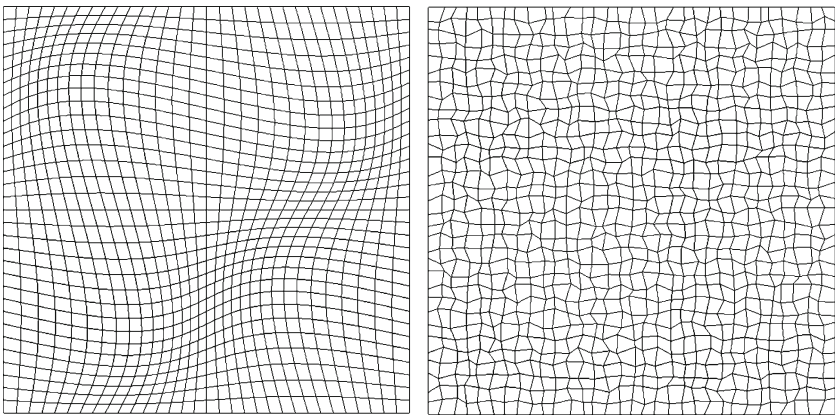

Fig. 5 Smooth quadrilateral mesh (*left*) and randomly h-perturbed quadrilateral mesh (*right*)

Table 1 Interpolation error $\|\mathbf{u} - \Pi\mathbf{u}\|_{\mathcal{F}_h}$ on the 2D meshes

$1/h$	Mesh 1		Mesh 2	
8	3.20E+0	–	3.43E+0	–
16	8.64E−1	1.89	9.30E−1	1.88
32	2.20E−1	1.97	2.47E−1	1.91
64	5.54E−2	1.99	5.34E−2	2.21
128	1.39E−2	1.99	1.38E−2	1.95
256	3.47E−3	2.00	3.80E−3	1.86
512	8.68E−4	2.00	8.86E−4	2.10

Table 2 Convergence in the 2D example on h^2-parallelogram grids

$1/h$	$\|p - p_h\|$		$\|\Pi\mathbf{u} - \mathbf{u}_h\|$		$\|\mathbf{u} - \mathbf{u}_h\|_{\mathcal{F}_h}$	
Symmetric MFMFE						
8	4.46E−1	–	1.04E+1	–	1.11E+1	–
16	2.02E−1	1.14	4.41E+0	1.24	4.12E+0	1.43
32	9.67E−2	1.06	2.19E+0	1.01	1.83E+0	1.17
64	4.79E−2	1.01	1.10E+0	0.99	8.86E−1	1.05
128	2.39E−2	1.00	5.50E−1	1.00	4.40E−1	1.01
256	1.19E−2	1.01	2.75E−1	1.00	2.19E−1	1.01
512	5.97E−3	1.00	1.38E−1	0.99	1.10E−1	1.00
Non-symmetric MFMFE						
8	4.45E−1	–	1.05E+1	–	1.10E+1	–
16	2.03E−1	1.13	4.38E+0	1.26	4.06E+0	1.44
32	9.67E−2	1.07	2.17E+0	1.01	1.81E+0	1.17
64	4.79E−2	1.01	1.09E+0	0.99	8.78E−1	1.04
128	2.39E−2	1.00	5.45E−1	1.00	4.36E−1	1.01
256	1.19E−2	1.01	2.73E−1	1.00	2.18E−1	1.00
512	5.97E−3	1.00	1.36E−1	1.01	1.09E−1	1.00

$1/h$	$\|\|\|p - p_h\|\|\|$		$\|\|\|\mathbf{u} - \mathbf{u}_h\|\|\|_{\mathcal{F}_h}$		$\|\|\|p - p_h\|\|\|$		$\|\|\|\mathbf{u} - \mathbf{u}_h\|\|\|_{\mathcal{F}_h}$	
Symmetric (left) and Non-symmetric (right) MFMFE								
8	2.37E−1	–	8.40E+0	–	2.35E−1	–	8.31E+0	–
16	4.96E−2	2.26	2.46E+0	1.77	4.99E−2	2.24	2.39E+0	1.80
32	1.15E−2	2.11	6.35E−1	1.95	1.16E−2	2.10	6.12E−1	1.97
64	2.84E−3	2.02	1.61E−1	1.98	2.86E−3	2.02	1.55E−1	1.98
128	7.08E−4	2.00	4.05E−2	1.99	7.12E−4	2.01	3.89E−2	1.99
256	1.77E−4	2.00	1.01E−2	2.00	1.78E−4	2.00	9.74E−3	2.00
512	4.42E−5	2.00	2.53E−3	2.00	4.45E−5	2.00	2.44E−3	2.00

MFMFE method [51] and the non-symmetric MFMFE method, we observe first order convergence for the pressure and the velocity. In addition, we obtain second order superconvergence for the face flux and the pressure at the cell centers.

Table 3 Convergence in the 2D example on randomly h-perturbed quadrilateral grids

$1/h$	$\|p - p_h\|$		$\|\Pi\mathbf{u} - \mathbf{u}_h\|$		$\|\mathbf{u} - \mathbf{u}_h\|_{\mathcal{F}_h}$	
Symmetric MFMFE						
8	6.02E−1	–	1.14E+1	–	1.32E+1	–
16	2.12E−1	1.51	4.86E+0	1.23	4.58E+0	1.53
32	9.95E−2	1.09	2.76E+0	0.82	2.47E+0	0.89
64	4.96E−2	1.00	1.94E+0	0.51	1.48E+0	0.74
128	2.51E−2	0.98	1.69E+0	0.20	1.34E+0	0.14
256	1.32E−2	0.93	1.60E+0	0.08	1.40E+0	<0
512	7.95E−3	0.73	1.60E+0	0.00	1.31E+0	0.10
Non-symmetric MFMFE						
8	6.04E−1	–	1.15E+1	–	1.28E+1	–
16	2.17E−1	1.48	4.77E+0	1.27	4.23E+0	1.60
32	1.00E−1	1.12	2.38E+0	1.00	1.95E+0	1.12
64	4.97E−2	1.01	1.19E+0	1.00	8.02E−1	1.28
128	2.48E−2	1.00	5.92E−1	1.01	4.07E−1	0.98
256	1.24E−2	1.00	2.97E−1	1.00	2.24E−1	0.86
512	6.20E−3	1.00	1.49E−1	1.00	1.05E−1	1.09

$1/h$	$\|\|p - p_h\|\|$		$\|\|\mathbf{u} - \mathbf{u}_h\|\|_{\mathcal{F}_h}$		$\|\|p - p_h\|\|$		$\|\|\mathbf{u} - \mathbf{u}_h\|\|_{\mathcal{F}_h}$	
Symmetric (left) and Non-symmetric (right) MFMFE								
8	3.51E−1	–	1.16E+1	–	3.48E−1	–	1.12E+1	–
16	6.42E−2	2.45	3.16E+0	1.88	7.14E−2	2.29	2.84E+0	1.98
32	1.35E−2	2.25	1.19E+0	1.41	1.33E−2	2.42	8.67E−1	1.71
64	5.21E−3	1.37	5.91E−1	1.01	3.15E−3	2.08	2.79E−1	1.64
128	4.94E−3	0.77	4.87E−1	0.28	7.58E−4	2.06	1.28E−1	1.12
256	4.88E−3	0.18	5.00E−1	<0	2.03E−4	1.90	6.86E−2	0.90
512	5.02E−3	<0	4.71E−1	0.09	4.83E−5	2.07	3.17E−2	1.11

Table 3 demonstrates the convergence behavior for the randomly perturbed grids of size $\mathcal{O}(h)$. The numerical results show that the non-symmetric MFMFE method has first order convergence for both the velocity and the pressure on these highly distorted grids. Clearly the convergence of the velocity and the pressure of the symmetric MFMFE method deteriorates.

5.2 3D examples

In the 3D examples we consider four hexahedral meshes. The first one is generated using a smooth map of a uniform grid given by

$$
\begin{aligned}
x &= \hat{x} + 0.03\sin(3\pi\hat{x})\cos(3\pi\hat{y})\cos(3\pi\hat{z}),\\
y &= \hat{y} - 0.04\cos(3\pi\hat{x})\sin(3\pi\hat{y})\cos(3\pi\hat{z}),\\
z &= \hat{z} + 0.05\cos(3\pi\hat{x})\cos(3\pi\hat{y})\sin(3\pi\hat{z}).
\end{aligned}
$$

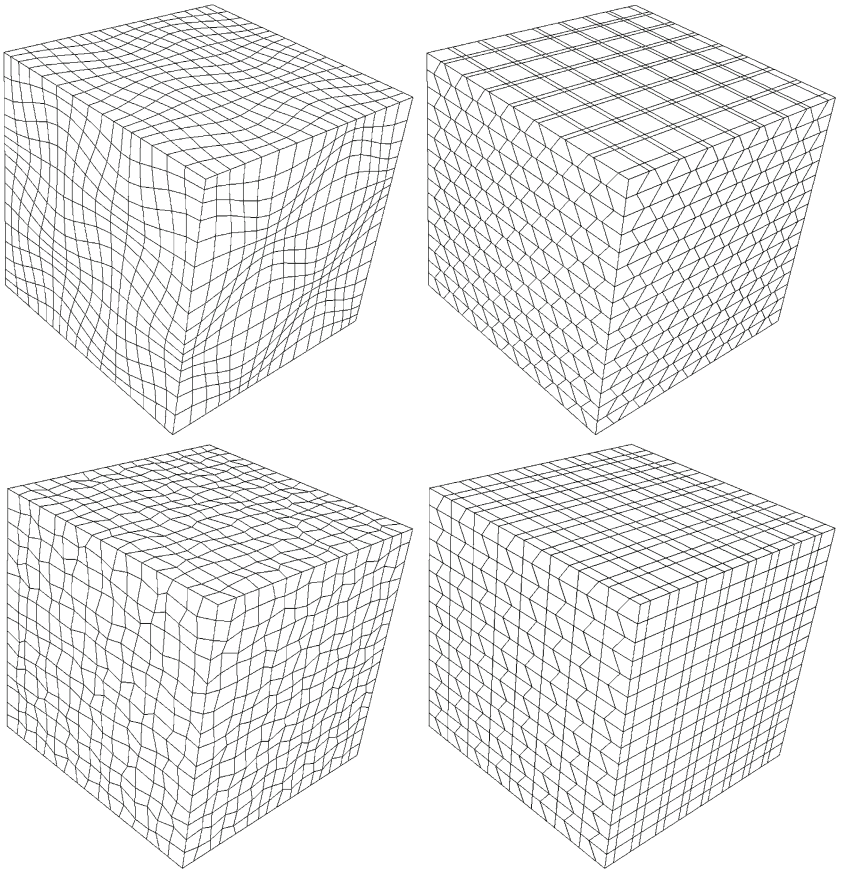

Fig. 6 The four 3D meshes: h^2-perturbed hexahedral mesh (*top-left*), h-perturbed mesh [43] (*top-right*), randomly h-perturbed hexahedral mesh (*bottom-left*), and h-perturbed mesh [29] (*bottom-right*)

This mapping yields an h^2-parallelepiped mesh. We choose the second mesh to be an h-perturbed grid given in [43]. The third mesh is generated by random perturbation of uniform mesh points by a distance of size $\mathcal{O}(h)$. The fourth mesh is a h-perturbed fish-bone-like mesh from [29]. Element faces are planar in the second mesh and non-planar in the other three meshes. The four meshes are shown in Fig. 6.

We consider problem (1.1)–(1.2) with a given analytical solution

$$p(x, y, z) = x^2(x-1)^2y^2(y-1)^2z^2(1-z)^2,$$

and a full permeability tensor

$$\mathbf{K} = \begin{pmatrix} \alpha & 1 & 1 \\ 1 & 2 & 1 \\ 1 & 1 & 2 \end{pmatrix},$$

where α is a parameter.

The convergence of the interpolation error $\|\mathbf{u} - \Pi\mathbf{u}\|_{\mathcal{F}_h}$, $\mathbf{u} = -K\nabla p$, on the four grids with $\alpha = 1$ is presented in Table 4. We observe first order convergence for the h-perturbed grids, as predicted by the theory. Moreover, second order convergence is obtained for the smooth grids. This can be proven by a scaling argument using the fact that the BDDF_1 interpolant preserves the normal components of linear vectors on the faces of the reference element. The scaling estimates developed in [33] for h^2-perturbed grids allow for the scaling argument to be employed without loss of accuracy. We note that such scaling argument would give no convergence on rough grids.

In order to explore the coercivity of the non-symmetric MFMFE method on distorted grids and anisotropic full tensor coefficients, we tested $\alpha = 10, 100, 1000$ on the four meshes. In some cases the coercivity condition (3.27) was violated, leading to a singular algebraic problem. For each mesh we report convergence for the largest value of α among the three tested, for which the non-symmetric method was positive definite. These values are $\alpha = 100$ for mesh one, $\alpha = 1000$ for mesh two, $\alpha = 10$ for mesh three, and $\alpha = 100$ for mesh four. As predicted by the theory in [33], the symmetric method was coercive in all cases. As we report below, the non-symmetric method exhibits first order convergence on all grids, while the convergence of the symmetric method deteriorates on rough grids. We note that one or the other method may be chosen element by element, depending on the roughness of the grid and the permeability anisotropy, as it is done in the coupled example in Sect. 5.3. Furthermore, there have been a number of modifications developed in the literature for the closely related MPFA method, which exhibit improved coercivity and monotonicity properties, such as methods with compact stencils [2,5] or increased pressure support [25,26]. These approaches, as well as grid smoothing techniques (Gridpro, http://www.gridpro.com/) or a posteriori error estimation and adaptive grid refinement [46], could be explored for the MFMFE method, but this is beyond the scope of this paper.

We also test the convergence of the symmetric and non-symmetric MFMFE methods on the randomly h-perturbed mesh 3 for a problem with a variable full tensor coefficient given by

$$\mathbf{K} = \begin{pmatrix} y^2 + 2 & \cos(xy) & \sin(xz) \\ \cos(xy) & (x+3)^2 & \cos(yz) \\ \sin(xz) & \cos(yz) & (x+1)^2 + z^2 \end{pmatrix}.$$

Table 4 Interpolation error $\|\mathbf{u} - \Pi\mathbf{u}\|_{\mathcal{F}_h}$ on the 3D meshes

$1/h$	Mesh 1		Mesh 2		Mesh 3		Mesh 4	
4	1.21E−4	–	1.67E−4	–	1.36E−4	–	1.60E−4	–
8	3.20E−5	1.92	7.20E−5	1.21	4.04E−5	1.75	5.65E−5	1.50
16	7.26E−6	2.14	3.40E−5	1.08	1.57E−5	1.36	2.29E−5	1.30
32	1.72E−6	2.08	1.69E−5	1.01	8.57E−6	0.87	1.06E−5	1.11
64	4.22E−7	2.03	8.51E−6	0.99	3.98E−6	1.11	5.21E−6	1.02
128	1.05E−7	2.01	4.28E−6	0.99	2.04E−6	0.96	2.59E−6	1.01

The pressure is as in the first four 3D examples.

Tables 5, 6, 7, 8 and 9 demonstrate the convergence behavior of both the symmetric and the non-symmetric MFMFE methods for the five examples described above.

The non-symmetric MFMFE method developed in this paper exhibits first order convergence for both velocity and pressure on all four meshes. These numerical results confirm the theory established in Theorems 3.1, 3.2, and 4.3. Furthermore, the computational results indicate second order superconvergence for pressure at the cell centers on all four meshes and for the face fluxes on the smooth mesh.

The symmetric MFMFE method on h^2-parallelepipeds has been proven to have first order convergence for velocity and pressure [33]. Table 5 confirms this theoretical result. We also observe similar convergence on the second and fourth meshes, see Tables 6 and 8, respectively. However, on the randomly perturbed mesh, the convergence of the velocity and the pressure in the symmetric MFMFE method deteriorates, see Tables 7 and 9.

5.3 A coupled scheme

Both the theory and the numerical examples confirm that the symmetric MFMFE method is accurate on h^2-parallelograms and h^2-parallelepipeds, and the non-symmetric MFMFE method is accurate on general quadrilateral and hexahedral grids. Recall that the distinction between these two methods lies in the numerical quadrature, which is defined at the element level. Thus the symmetric and the non-symmetric MFMFE

Table 5 Convergence in the first 3D example on smooth hexahedral grids with $\alpha = 100$

$1/h$	$\|p - p_h\|$		$\|\Pi\mathbf{u} - \mathbf{u}_h\|$		$\|\mathbf{u} - \mathbf{u}_h\|_{\mathcal{F}_h}$	
Symmetric MFMFE						
8	1.48E−05	–	5.15E−03	–	3.82E−03	–
16	7.17E−06	1.05	2.77E−03	0.89	1.80E−03	1.09
32	3.56E−06	1.01	1.43E−03	0.95	8.67E−04	1.05
64	1.78E−06	1.00	7.25E−04	0.98	4.30E−04	1.01
Non-symmetric MFMFE						
8	1.48E−05	–	5.74E−03	–	4.37E−03	–
16	7.19E−06	1.04	2.56E−03	1.06	1.67E−03	1.39
32	3.56E−06	1.01	1.25E−03	1.03	7.59E−04	1.14
64	1.78E−06	1.00	6.26E−04	1.00	3.71E−04	1.03

$1/h$	$\|\|\|p - p_h\|\|\|$		$\|\|\|\mathbf{u} - \mathbf{u}_h\|\|\|_{\mathcal{F}_h}$		$\|\|\|p - p_h\|\|\|$		$\|\|\|\mathbf{u} - \mathbf{u}_h\|\|\|_{\mathcal{F}_h}$	
Symmetric (left) and Non-symmetric (right) MFMFE								
8	4.12E−06	–	1.31E−03	–	3.87E−06	–	1.58E−03	–
16	1.05E−06	1.97	4.59E−04	1.51	1.04E−06	1.90	4.08E−04	1.95
32	2.69E−07	1.96	1.27E−04	1.85	2.68E−07	1.96	1.01E−04	2.01
64	6.84E−08	1.98	3.37E−05	1.91	6.77E−08	1.99	2.57E−05	1.97

Table 6 Second 3D example on an h-perturbed grid with $\alpha = 1000$

$1/h$	$\|p - p_h\|$		$\|\Pi\mathbf{u} - \mathbf{u}_h\|$		$\|\mathbf{u} - \mathbf{u}_h\|_{\mathcal{F}_h}$	
Symmetric MFMFE						
8	1.57E−05	–	9.38E−02	–	5.70E−02	–
16	7.83E−06	1.00	4.97E−02	0.92	2.91E−02	0.97
32	3.90E−06	1.01	2.60E−02	0.93	1.50E−02	0.96
64	1.95E−06	1.00	1.33E−02	0.97	7.69E−03	0.96
Non-symmetric MFMFE						
8	1.57E−05	–	9.70E−02	–	5.80E−02	–
16	7.81E−06	1.01	5.17E−02	0.91	3.00E−02	0.95
32	3.90E−06	1.00	2.66E−02	0.96	1.54E−02	0.96
64	1.95E−06	1.00	1.35E−02	0.98	7.79E−03	0.98

$1/h$	$\|\|\|p - p_h\|\|\|$		$\|\|\|\mathbf{u} - \mathbf{u}_h\|\|\|_{\mathcal{F}_h}$		$\|\|\|p - p_h\|\|\|$		$\|\|\|\mathbf{u} - \mathbf{u}_h\|\|\|_{\mathcal{F}_h}$	
Symmetric (left) and Non-symmetric (right) MFMFE								
8	3.06E−06	–	2.35E−02	–	2.64E−06	–	2.29E−02	–
16	9.15E−07	1.74	9.91E−03	1.25	6.87E−07	1.94	9.79E−03	1.23
32	2.47E−07	1.89	4.76E−03	1.06	1.76E−07	1.96	4.76E−03	1.04
64	6.13E−08	2.01	2.39E−03	0.99	4.53E−08	1.96	2.39E−03	0.99

Table 7 Third 3D example on a randomly h-perturbed grid with $\alpha = 10$

$1/h$	$\|p - p_h\|$		$\|\Pi\mathbf{u} - \mathbf{u}_h\|$		$\|\mathbf{u} - \mathbf{u}_h\|_{\mathcal{F}_h}$	
Symmetric MFMFE						
8	1.49E−05	–	7.16E−04	–	5.25E−04	–
16	7.27E−06	1.04	4.71E−04	0.60	3.25E−04	0.69
32	3.82E−06	0.93	3.75E−04	0.33	3.09E−04	0.07
64	2.31E−06	0.73	3.48E−04	0.11	2.76E−04	0.16
Non-symmetric MFMFE						
8	1.50E−05	–	7.29E−04	–	5.37E−04	–
16	7.21E−06	1.06	3.75E−04	0.96	2.59E−04	1.05
32	3.57E−06	1.01	1.88E−04	1.00	1.52E−04	0.77
64	1.78E−06	1.00	9.45E−05	0.99	7.32E−05	1.05

$1/h$	$\|\|\|p - p_h\|\|\|$		$\|\|\|\mathbf{u} - \mathbf{u}_h\|\|\|_{\mathcal{F}_h}$		$\|\|\|p - p_h\|\|\|$		$\|\|\|\mathbf{u} - \mathbf{u}_h\|\|\|_{\mathcal{F}_h}$	
Symmetric (left) and Non-symmetric (right) MFMFE								
8	3.79E−06	–	2.26E−04	–	3.64E−06	–	2.42E−04	–
16	1.73E−06	1.13	1.17E−04	0.95	1.02E−06	1.84	8.01E−05	1.60
32	1.47E−06	0.24	1.17E−04	0.00	2.63E−07	1.96	3.84E−05	1.06
64	1.49E−06	<0	1.10E−04	0.09	6.62E−08	1.99	1.73E−05	1.15

Table 8 Fourth 3D example on an h-perturbed grid with $\alpha = 100$

$1/h$	$\|p - p_h\|$		$\|\Pi\mathbf{u} - \mathbf{u}_h\|$		$\|\mathbf{u} - \mathbf{u}_h\|_{\mathcal{F}_h}$	
Symmetric MFMFE						
8	1.53E−05	–	7.39E−03	–	6.27E−03	–
16	7.38E−06	1.05	3.79E−03	0.96	3.15E−03	0.99
32	3.65E−06	1.02	1.91E−03	0.99	1.59E−03	0.99
64	1.82E−06	1.00	9.57E−04	1.00	7.96E−04	1.00
Non-symmetric MFMFE						
8	1.52E−05	–	7.40E−03	–	6.33E−03	–
16	7.36E−06	1.05	3.81E−03	0.96	3.17E−03	1.00
32	3.65E−06	1.01	1.92E−03	0.99	1.59E−03	1.00
64	1.82E−06	1.00	9.62E−04	1.00	7.97E−04	1.00

$1/h$	$\|\|\|p - p_h\|\|\|$		$\|\|\|\mathbf{u} - \mathbf{u}_h\|\|\|_{\mathcal{F}_h}$		$\|\|\|p - p_h\|\|\|$		$\|\|\|\mathbf{u} - \mathbf{u}_h\|\|\|_{\mathcal{F}_h}$	
Symmetric (left) and Non-symmetric (right) MFMFE								
8	3.97E−06	–	2.22E−03	–	3.64E−06	–	2.21E−03	–
16	1.04E−06	1.93	8.14E−04	1.45	1.01E−06	1.85	7.51E−04	1.56
32	2.57E−07	2.02	3.86E−04	1.08	2.83E−07	1.84	3.27E−04	1.20
64	6.30E−08	2.03	1.97E−04	0.97	9.28E−08	1.61	1.60E−04	1.03

Table 9 Fifth 3D example on a randomly h-perturbed grid with a variable permeability

$1/h$	$\|p - p_h\|$		$\|\Pi\mathbf{u} - \mathbf{u}_h\|$		$\|\mathbf{u} - \mathbf{u}_h\|_{\mathcal{F}_h}$	
Symmetric MFMFE						
8	1.48E−05	–	9.15E−04	–	6.61E−04	–
16	7.26E−06	1.03	5.87E−04	0.64	4.06E−04	0.70
32	3.82E−06	0.93	4.64E−04	0.34	3.83E−04	0.08
64	2.30E−06	0.73	4.30E−04	0.11	3.40E−04	0.17
Non-symmetric MFMFE						
8	1.49E−05	–	9.23E−04	–	6.66E−04	–
16	7.20E−06	1.05	4.68E−04	0.98	3.21E−04	1.05
32	3.57E−06	1.01	2.36E−04	0.99	1.90E−04	0.76
64	1.78E−06	1.00	1.18E−04	1.00	9.11E−05	1.07

$1/h$	$\|\|\|p - p_h\|\|\|$		$\|\|\|\mathbf{u} - \mathbf{u}_h\|\|\|_{\mathcal{F}_h}$		$\|\|\|p - p_h\|\|\|$		$\|\|\|\mathbf{u} - \mathbf{u}_h\|\|\|_{\mathcal{F}_h}$	
Symmetric (left) and Non-symmetric (right) MFMFE								
8	3.54E−06	–	2.65E−04	–	3.37E−06	–	2.78E−04	–
16	1.70E−06	1.06	1.35E−04	0.97	9.92E−07	1.76	8.83E−05	1.65
32	1.48E−06	0.20	1.39E−04	<0	2.54E−07	1.97	3.98E−05	1.15
64	1.49E−06	<0	1.31E−04	0.09	6.41E−08	1.99	1.71E−05	1.22

methods can be easily coupled element by element. In particular, one can select the symmetric quadrature rule for h^2-perturbed elements and the non-symmetric quadrature rule for highly distorted elements. To test this concept, we choose the "coupled" mesh as shown in Fig. 7 consisting of the randomly h-perturbed and the h^2-perturbed meshes from Fig. 5, as well as a uniform mesh. The analytical solution, permeability, and boundary condition are the same as in Sect. 5.1. Table 10 demonstrates that the coupled method has first order convergence for the pressure and the velocity and has second order convergence for the pressure at the cell centers.

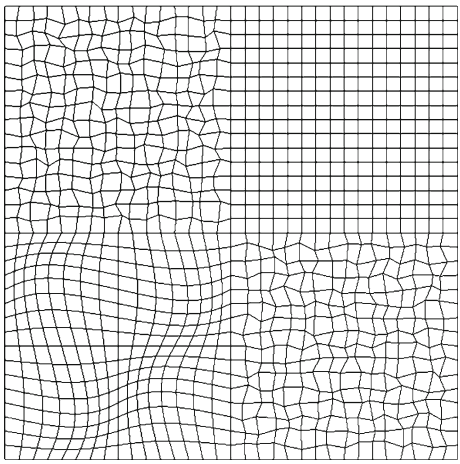

Fig. 7 A "coupled" mesh consists of h^2-perturbed and randomly h-perturbed quadrilaterals, and uniform rectangles

Table 10 Symmetric MFMFE coupled with Non-symmetric MFMFE

$1/h$	$\|p - p_h\|$		$\|\Pi\mathbf{u} - \mathbf{u}_h\|$		$\|\mathbf{u} - \mathbf{u}_h\|_{\mathcal{F}_h}$	
4	3.40E+0	–	4.52E+1	–	5.86E+1	–
8	5.96E−1	2.51	1.02E+1	2.15	1.18E+1	2.31
16	2.03E−1	1.55	4.37E+0	1.22	4.00E+0	1.56
32	9.72E−2	1.06	2.16E+0	1.02	1.75E+0	1.19
64	4.79E−2	1.02	1.11E+0	0.96	8.58E−1	1.03
128	2.39E−2	1.00	5.53E−1	1.01	4.25E−1	1.01
256	1.20E−2	0.99	2.77E−1	1.00	2.13E−1	1.00
$1/h$	$\|\|\|p - p_h\|\|\|$		$\|\|\|\mathbf{u} - \mathbf{u}_h\|\|\|_{\mathcal{F}_h}$			
4	3.04E+0	–	5.47E+1	–		
8	3.96E−1	2.94	9.82E+0	2.48		
16	4.77E−2	3.05	2.49E+0	1.98		
32	1.17E−2	2.03	7.07E−1	1.82		
64	2.91E−3	2.01	2.39E−1	1.56		
128	7.73E−4	1.91	1.00E−1	1.26		
256	1.84E−4	2.07	4.75E−2	1.07		

6 Conclusions

In this paper, a non-symmetric MFMFE method on both quadrilaterals and hexahedra is developed based on BDM_1 and enhanced $BDDF_1$ spaces, and a special quadrature rule. This method gives a cell-centered pressure stencil by locally eliminating the velocity degrees of freedom. On highly distorted quadrilateral and hexahedral grids, the non-symmetric MFMFE method gives better approximation than the symmetric formulation from [33,51]. In particular, the non-symmetric MFMFE method exhibits first order convergence for pressure and normal velocities on faces, as well as second order superconvergence for the pressure at the cell centers. Furthermore, second order superconvergence is observed for the face fluxes on smooth meshes. The method can handle non-planar hexahedral faces. Since the symmetric and non-symmetric MFMFE methods are locally defined, they can be coupled so that the non-symmetric method is applied to highly distorted elements. Affine elements can also be coupled with quadrilateral and hexahedral elements. We remark that based on accurate velocities on faces one can obtain accurate velocity inside elements by applying post-processing techniques [49].

Acknowledgments Mary Wheeler is supported by the NSF-CDI under contract number DMS 0835745, the DOE grant DE-FG02-04ER25617, and the Center for Frontiers of Subsurface Energy Security under Contract No. DE-SC0001114. Guangri Xue is supported by Award No. KUS-F1-032-04, made by King Abdullah University of Science and Technology (KAUST). Ivan Yotov is partially supported by the DOE grant DE-FG02-04ER25618, the NSF grant DMS 0813901, and the J. Tinsley Oden Faculty Fellowship, ICES, The University of Texas at Austin.

References

1. Aavatsmark, I., Eigestad, G.T., Klausen, R.A., Wheeler, M.F., Yotov, I.: Convergence of a symmetric MPFA method on quadrilateral grids. Comput. Geosci. **11**, 333–345 (2007)
2. Aavatsmark, I., Eigestad, G.T., Mallison, B.T., Nordbotten, J.M.: A compact multipoint flux approximation method with improved robustness. Numer. Methods Partial Differ. Equ. **24**, 1329–1360 (2008)
3. Aavatsmark, I.: An introduction to multipoint flux approximations for quadrilateral grids. Comput. Geosci. **6**, 405–432 (2002)
4. Aavatsmark, I., Barkve, T., Boe, O., Mannseth, T.: Discretization on unstructured grids for inhomogeneous, anisotropic media. Part II: discussion and numerical results. SIAM J. Sci. Comput. **19**, 1717–1736 (1998)
5. Aavatsmark, I., Eigestad, G.T., Heigsund, B.-O., Mallison, B.T., Nordbotten, J.M., Oian, E.: A new finite-volume approach to efficient discretization on challenging grids. SPE J. **15**, 658–669 (2010)
6. Agmon, S.: Lectures on Elliptic Boundary Value Problems. Van Nostrand, Princeton (1965)
7. Arbogast, T., Dawson, C.N., Keenan, P.T., Wheeler, M., Yotov, I.: Enhanced cell-centered finite differences for elliptic equations on general geometry. SIAM J. Sci. Comput. **19**, 404–425 (1998)
8. Arbogast, T., Wheeler, M., Yotov, I.: Mixed finite elements for elliptic problems with tensor coefficients as cell-centered finite differences. SIAM J. Numer. Anal. **34**, 828–852 (1997)
9. Arnold, D.N.: An interior penalty finite element method with discontinuous elements. SIAM J. Numer. Anal. **19**, 742–760 (1982)
10. Arnold, D.N., Boffi, D., Falk, R.S.: Approximation by quadrilateral finite elements. Math. Comput. **71**, 909–922 (2002)
11. Arnold, D.N., Boffi, D., Falk, R.S.: Quadrilateral H(div) finite elements. SIAM J. Numer. Anal. **42**, 2429–2451 (2005)
12. Arnold, D.N., Brezzi, F.: Mixed and nonconforming finite element methods: implementation, postprocessing and error estimates. Math. Mod. Numer. Anal. **19**, 7–32 (1985)

13. Brenner, S.C., Scott, L.R.: The Mathematical Theory of Finite Element Methods. Texts in Applied Mathematics. Springer, Berlin (2007)
14. Brezzi, F., Douglas, J., Duran, R., Fortin, M.: Mixed finite elements for second order elliptic problems in three variables. Numer. Math. **51**, 237–250 (1987)
15. Brezzi, F., Douglas, J., Marini, L.D.: Two families of mixed finite elements for second order elliptic problems. Numer. Math. **47**, 217–235 (1985)
16. Brezzi, F., Fortin, M.: Mixed and Hybrid Finite Element Methods. Springer, New York (1991)
17. Brezzi, F., Fortin, M., Marini, L.D.: Error analysis of piecewise constant pressure approximations of Darcy's law. Comput. Methods Appl. Mech. Eng. **195**, 1547–1559 (2006)
18. Brezzi, F., Lipnikov, K., Shashkov, M.: Convergence of mimetic finite difference method for diffusion problems on polyhedral meshes. SIAM J. Numer. Anal. **43**, 1872–1896 (2005)
19. Brezzi, F., Lipnikov, K., Shashkov, M.: Convergence of mimetic finite difference method for diffusion problems on polyhedral meshes with curved faces. Math. Mod. Methods. Appl. Sci. **16**, 275–297 (2006)
20. Chen, Z., Douglas, J.: Prismatic mixed finite elements for second order elliptic problems. Calcolo **26**, 135–148 (1989)
21. Ciarlet, P.G.: The Finite Element Method for Elliptic Problems. Stud. Math. Appl., vol. 4, North-Holland, Amsterdam, 1978; Reprinted, SIAM, Philadelphia (2002)
22. Douglas, J., Wang, J.: A new family of mixed finite element spaces over rectangles. Math. Appl. Comput. **12**, 183–197 (1993)
23. Edwards, M.G.: Unstructured control-volume distributed, full-tensor finite-volume schemes with flow based grids. Comput. Geosci. **6**, 433–452 (2002)
24. Edwards, M.G., Rogers, C.F.: Finite volume discretization with imposed flux continuity for the general tensor pressure equation. Comput. Geosci. **2**, 259–290 (1998)
25. Edwards, M.G., Zheng, H.: Double-families of quasi-positive Darcy-flux approximations with highly anisotropic tensors on structured and unstructured. J. Comput. Phys. **229**, 594–625 (2010)
26. Edwards, M.G., Zheng, H.: Quasi M-matrix multifamily continuous Darcy-flux approximations with full pressure support on structured and unstructured grids in three dimensions. SIAM J. Sci. Comput. **33**, 455–487 (2011)
27. Ewing, R.E., Liu, M.M., Wang, J.: Superconvergence of mixed finite element approximations over quadrilaterals. SIAM. J. Numer. Anal. **36**, 772–787 (1999)
28. Eymard, R., Gallouët, T., Herbin, R.: Finite volume methods. In: Handbook of Numerical Analysis, vol. VII, pp. 713–1020. North-Holland, Amsterdam (2000)
29. Falk, R.S., Gatto, P., Monk, P.: Hexahedral H(div) and H(curl) finite elements. Math. Mod. Numer. Anal. (2010, to appear)
30. Galdi, G.P.: An Introduction to the Mathematical Theory of the Navier-Stokes equations. vol. I. Linearized Steady Problems. Springer, New York (1994)
31. Girault, V., Raviart, P.A.: Finite Element Methods for Navier-Stokes Equations, Theory and Algorithms. Springer, Berlin (1986)
32. Hyman, J., Shashkov, M., Steinberg, S.: The numerical solution of diffusion problem in strongly heterogeneous non-isotropic materials. J. Comput. Phys. **132**, 130–148 (1997)
33. Ingram, R., Wheeler, M., Yotov, I.: A multipoint flux mixed finite element method on hexahedra. SIAM J. Numer. Anal. **48**, 1281–1312 (2010)
34. Klausen, R.A., Winther, R.: Convergence of multipoint flux approximations on quadrilateral grids. Numer. Methods Partial Differ. Equ. **22**, 1438–1454 (2006)
35. Klausen, R.A., Winther, R.: Robust convergence of multi point flux approximation on rough grids. Numer. Math. **104**, 317–337 (2006)
36. Kuznetsov, Y., Repin, S.: Convergence analysis and error estimates for mixed finite element method on distorted meshes. J. Numer. Math. **13**, 33–51 (2005)
37. Lipnikov, K., Shashkov, M., Yotov, I.: Local flux mimetic finite difference methods. Numer. Math. **112**, 115–152 (2009)
38. Marsden, J.E., Hughes, T.J.: Mathematical Foundations of Elasticity. Prentice-Hall, Englewood Cliffs (1983)
39. Naff, R., Russell, T., Wilson, J.D.: Shape functions for velocity interpolation in general hexahedral cells. Comput. Geosci. **6**, 285–314 (2002)
40. Nedelec, J.C.: Mixed finite elements in R^3. Numer. Math. **35**, 315–341 (1980)

41. Raviart, P.A., Thomas, J.M.: A mixed finite element method for 2-nd order elliptic problems. In: Galligani, I., Magenes, E. (eds.) Mathematical Aspects of the Finite Elements Method. Lectures Notes in Math., vol. 606, pp. 292–315. Springer, Berlin (1977)
42. Russell, T., Wheeler, M.: Finite element and finite difference method for continuous flows in porous media. Front. Appl. Math. **1**, 35–106 (1983)
43. Sboui, A., Jaffre, J., Roberts, J.: A composite mixed finite elements for hexahedral grids. SIAM. J. Sci. Comput. **31**, 2623–2645 (2009)
44. Shen, J.: Mixed finite element methods on distorted rectangular grids. Technical report, Texas A & M University (1994)
45. Thomas, J.M.: These de Doctorat d'etat. 'a l'Universite Pierre et Marie Curie, Paris (1977)
46. Vohralík, M.: Residual flux-based a posteriori error estimates for finite volume and related locally conservative methods. Numer. Math. **111**, 121–158 (2008)
47. Wang, J., Mathew, T.: Mixed finite element method over quadrilaterals. In: Advances in Numerical Methods and Applications: Proceedings of Third International Conference, pp. 203–214. World Scientific, River Edge (1994)
48. Weiser, A., Wheeler, M.: On convergence of block-centered finite differences for elliptic problems. SIAM J. Numer. Anal. **25**, 351–375 (1988)
49. Wheeler, M., Xue, G., Yotov, I.: Local velocity postprocessing for multipoint flux methods on general hexahedra. Int. J. Numer. Anal. Model. (2011, accepted)
50. Wheeler, M., Xue, G., Yotov, I.: A multiscale mortar multipoint flux mixed finite element method. Math. Model. Numer. Anal. (2011, accepted)
51. Wheeler, M., Yotov, I.: A multipoint flux mixed finite element method. SIAM. J. Numer. Anal. **44**, 2082–2106 (2006)